Heliyon 10 (2024) e39083

Contents lists available at ScienceDirect

Heliyon

journal homepage: www.cell.com/heliyon

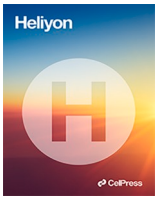

Research article

Physical and electrochemical performances of novel tellurium composite films as anode applications in energy storage systems

Md Masud Rana [a,*], Mohammad Asaduzzaman Chowdhury [a], Md. Jonaidul Alam [a], Md. Rifat Khandaker [b], Yusuf Ali [a]

[a] Department of Mechanical Engineering, Dhaka University of Engineering and Technology (DUET), Gazipur, Gazipur, 1707, Bangladesh
[b] Department of Chemical Engineering, Dhaka University of Engineering and Technology (DUET), Gazipur, Gazipur, 1707, Bangladesh

ARTICLE INFO

Keywords:
Tellurium composite
Anode
Physiochemical properties
Thermal analysis
Energy storage

ABSTRACT

Portable electronic devices and electric cars use lithium-ion batteries, but clumping lithium alloys limit their lifespan. Due to their strong electronic conductivity, volumetric capacity, and high energy density, researchers are conducting research on electrochemical metal cells utilizing tellurium for high-performance batteries. Theoretically, lithium-tellurium batteries can improve energy densities three times more than lithium-ion batteries. However, metal-tellurium faces challenges such as low rate capability, unclear redox reactions, intermediate dissolution, and electrode volume changes. This study explores the enhancement of the energy storage capacity of next-generation batteries by fabricating coated electrode films as novel anodes from tellurium, silicon, and graphene. Physical, thermal, and morphological analysis of composite material are investigated by XRD, TEM, TGA, DSC, SEM, UV, and XPS analyses, revealing its rigidity as well as durability through its crystal structure alignment and thermal stability. In electrochemical analysis (CV) at various scan rates, samples that exhibit consistent and high specific capacity (Cp) values at different scan speeds (25, 50, and 100 mV/s) indicate excellent ability to store and maintain charge. Decreasing Cp values with increasing scan rates indicate that the speed of cycling limits the charge transfer kinetics and electrode performance. In EIS, the charge transfer resistances (R_{ct}) for the pure Te, Te + Gr, Te + Si + Gr, and Te + Si samples are 759.07 Ω, 4.21 Ω, 36.39 Ω, and 164.90 Ω, respectively. The Te + Gr sample has the lowest R_{ct}, indicating the best charge transfer efficiency at the electrode contact, whereas the Te + Si + Gr sample has a comparatively lower R_{ct}, indicating better charge transfer kinetics. The combined result exhibits the synergistic impact of tellurium, silicon, and graphene in enhancing the energy storage capacity of future batteries across the industry.

1. Introduction

The exhaustion of fossil fuels and severe environmental contamination are prompting the exploration of alternate energy sources, including the advancement of environmentally sustainable energy sources, which are growing rapidly [1,2]. Furthermore, there has been ongoing discourse regarding the widespread adoption of intelligent devices and high-capacity energy storage devices, such as

* Corresponding author.
E-mail addresses: masudranadeepto@gmail.com (M.M. Rana), asadzmn2014@yahoo.com (M.A. Chowdhury), jonaid@duet.ac.bd (Md.J. Alam), rifatkh.duet@gmail.com (Md.R. Khandaker), bizonkhan@gmail.com (Y. Ali).

https://doi.org/10.1016/j.heliyon.2024.e39083
Received 24 July 2024; Received in revised form 7 October 2024; Accepted 7 October 2024
Available online 9 October 2024
2405-8440/© 2024 The Authors. Published by Elsevier Ltd. This is an open access article under the CC BY-NC license (http://creativecommons.org/licenses/by-nc/4.0/).

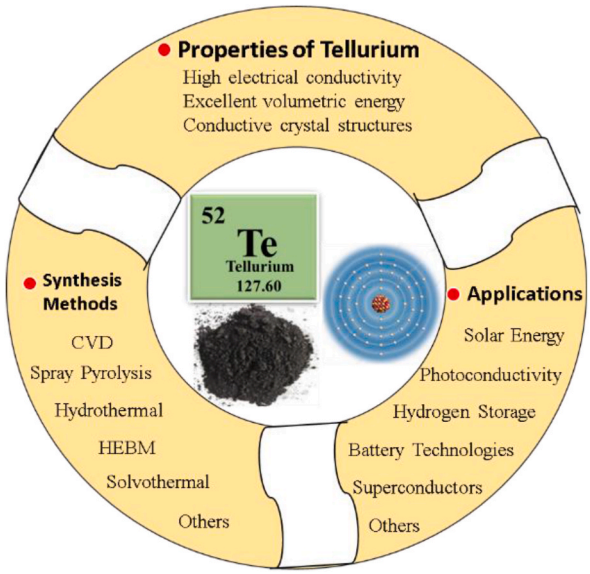

Fig. 1. Symmetric diagram of Tellurium Properties, Synthesis Methods, and Applications.

energy storage systems and electric vehicles [3,4]. In this context, there is a growing demand for lithium-ion batteries (LIBs) that possess a large capacity, high energy density, and a long lifespan [5,6]. Ongoing research is focused on optimizing the anode material in LIBs, as it has a substantial impact on battery capacity and charge/discharge speed [6,7].

At now, graphite is predominantly utilized as the anode material because of its affordability and strong durability. Nevertheless, it is worth noting that it suffers from the drawback of a very low theoretical capacity of 372 mAh/g [8–10]. Research into high-capacity anodes that can replace graphite is actively being done due to the increasing need for high-energy-density batteries [11,12].

Among the different alloy anodes, chalcogen groups (S, Se, and Te) [13,14] from Group 16 of the periodic table have been extensively studied. Te exhibits a higher electronic conductivity of 2.0102 S/m, surpassing that of Se (1.010−4 S/m) and S (5.010−16 S/m) [13]. Theoretically, tellurium has a larger volumetric capacity of 2621 mAh/cm^3 compared to graphite anodes. This is due to its high density of 6.24 g/cm^3. The high density of the battery provides the benefits of minimizing the space taken up by the battery within the device and the need for extra materials [15,16].

Tellurium (Te) has undergone thorough investigation in not just LIBs but also in different types of ionic batteries, including sodium-ion batteries (SIBs) and potassium batteries utilizing carbonaceous materials. A composite material consisting of nanostructured tellurium and carbon for use in SIBs [17,18]. However, Tellurium exhibits increased brittleness due to its inherent brittleness at normal room temperature [19]. In addition, high temperatures enhance the rate of chemical reactions and volume expansion, resulting in a decrease in the overall efficiency of tellurium [20].

Silicon has a theoretical capacity of over 4200 mAh/g [21,22], which is far higher than graphite's 372 mAh/g [22], it is a strong contender for improving battery performance. During cycles of charging and discharging, silicon has a greater potential to collect and release lithium ions, increasing its energy storage capacity [23]. A variety of techniques, including the use of silicon nanoparticles, and silicon-graphene composites, are used in the development of silicon-based anode materials [24,25]. By reducing the difficulties brought on by silicon's significant volume expansion during cycling [26,27], each of these architectures seeks to increase the battery's overall stability and longevity.

Fig. 1 shows the symmetric diagram of tellurium properties, synthesis methods, and applications. Tellurium has great prospects in energy storage systems, however, tellurium exhibits major limitations of intermediate dissolution and volume expansion during cycling [28].

In this study, to fabricate novel tellurium-based composite films as anode combined with graphene and silicon for resolving the individual limitations tellurium, graphene and silicon. Graphene has remarkable mechanical stability and flexibility as a result of its outstanding tensile strength and elasticity. While both tellurium and silicon experience substantial variations in volume during the cycling process, the use of a composite material combining these two elements successfully reduces these limits. The Te-Si composite utilizes the distinct expansion characteristics of each material to uniformly distribute and absorb mechanical stress. The composite structure formed by combining silicon and tellurium takes use of silicon's high capacity and greater volume expansion while being counterbalanced by tellurium's relatively lower expansion. This combination allows the structure to effectively tolerate overall volume changes. In addition, graphene and silicon are associated with the movement of electrons, reduce the electrical resistance, and boost the overall efficiency of the tellurium. This is confirmed by the physiochemical tests. During physiochemical analysis (CV and EIS) of composite films, the higher specific capacity and lower charge transfer resistance (R_{ct}) are evaluated, which is promising for anode applications in energy storage systems.

Table 1
The weight percentage and material composition of fabricated samples.

Sample name	Tellurium (wt. %)	Graphene (wt. %)	Silicon (wt. %)
Pure Te (S1)	100	–	–
Te + Gr (S2)	60	40	–
Te + Si + Gr (S3)	60	10	30
Te + Si (S4)	60	–	40

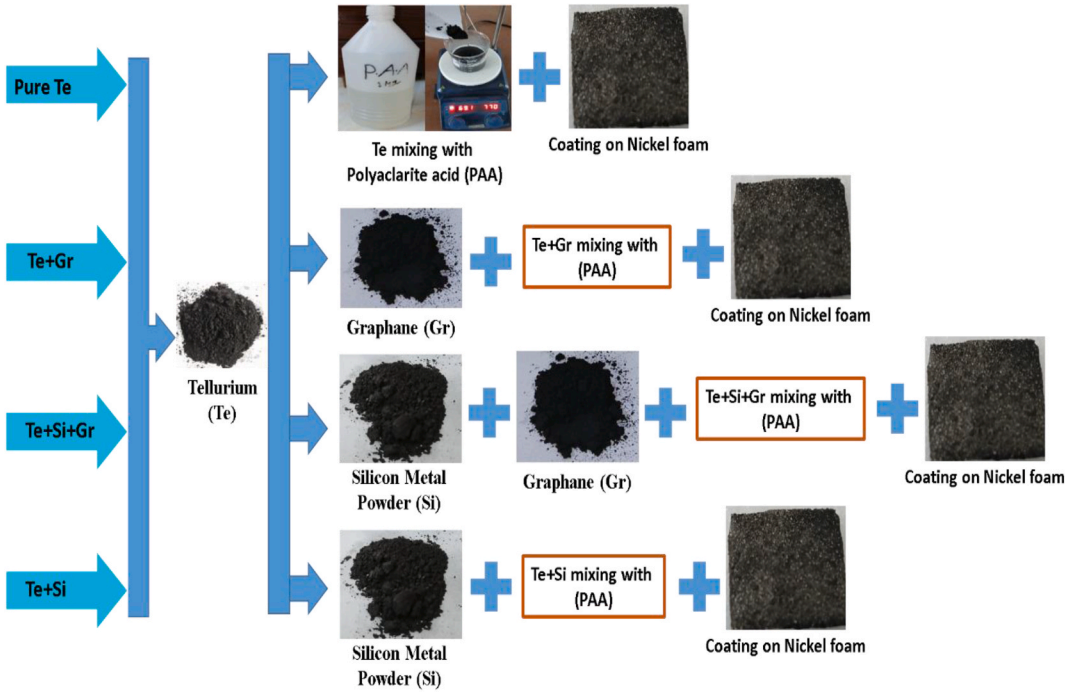

Fig. 2. Fabrication process of anode.

2. Experimental methods

2.1. Materials

This study, three different types of materials are used to make four types of samples: tellurium (Te) powder (25 g, 200 mesh, 99.8 % trace metal basis, Sigma-Aldrich, Co., 3050 Spruce Street, St. Louis, MO 63103 USA), graphene (Gr) (nanoparticle purity 99 %). Thickness: 5–10 nm (CAS No.: 7782-42-5 Mol. Wet: 12.01 Rjapalya, Hoodi, Bangalore-560048) and silicon (Si) metal powder (200 mesh, 98.5 % extra pure). MF-Si, MW-28.09, Assay-Min 98.5 %, Mumbai (India)). However, polyacrylic acid solvent (water, concentration: 2 % (w/v), electrolyte compatibility: organic.) was used for slurry making and this slurry was coated on the Nickel foam electrode.

2.2. Anode preparation

The anode preparation the weight percentage compositions of four samples are as follows: the first sample, tellurium 100 % (wt%); the second sample, tellurium 60 % (wt%) with graphene 40 % (wt%); the third sample, tellurium 60 % (wt%) with graphene 10 % (wt %) and silicon 30 %; and the fourth sample, tellurium 60 % (wt%) with silicon 40 %. Table 1 shows the weight percentage and material composition of these samples. All the samples were homogeneously mixed and fine powdered using a mortar and pestle. They were mixed with a polyacrylic acid (PAA) liquid binder solution and stirred until they formed a slurry.

Nickel foam (thickness: 1 mm, size and shape: 500*500mm/200*300 mm, porosity: 95%–98 %) is collected from China. The nickel foam serves as a current collector for anode materials. Coated nickel foam electrodes of Area = 25 × 25 mm^2 Thickness = 1 mm undergo the dip-coating process [29]. This process is an economical, dependable, and reproducible technique wherein a moist liquid film is deposited onto a substrate through its withdrawal at a consistent velocity into a vapor-filled atmosphere after its immersion in a sample solution. After completing the process, all coated samples were dried in the oven at 100 °C. The process of sample preparation is illustrated in Fig. 2.

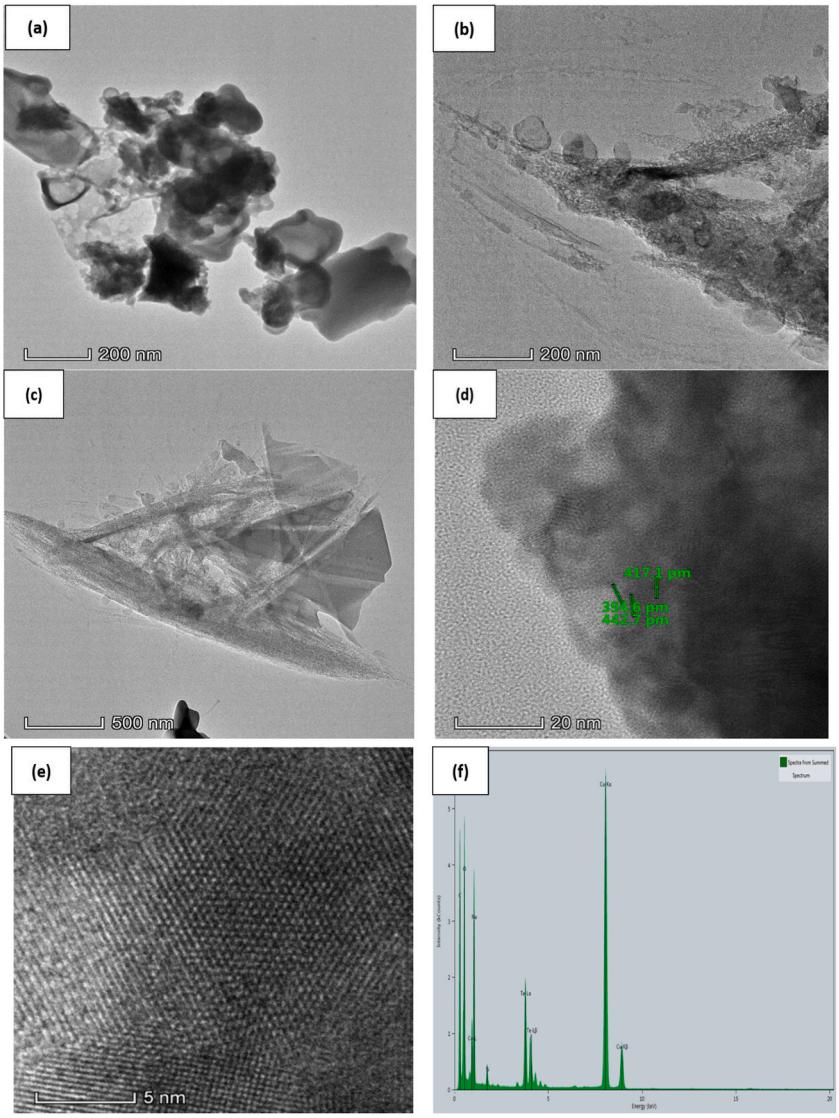

Fig. 3. Pure Te sample (a, b, c) TEM image (d) Crystal Structure with interplanar spacing (e) Crystal Structure (f) EDX spectrum.

2.3. Theoretical capacity and ion storage mechanisms of tellurium composite films

The theoretical capacity is the maximum charge it can store per unit mass when used as an electrode in a battery. The data below illustrates the theoretical capacities for tellurium.

F0B7 **Molar Mass of Tellurium (Te):** 127.6 g/mol
F0B7 **Number of Electrons (n)**: 2 electrons per Te atom
F0B7 **Faraday's Constant (F)**: 26.8 Ah/mol (96,485C/mol)

$$C = \frac{n \times F}{Molar\ mass\ of\ Te} = \frac{2 \times 26.8}{127.6} = 420\ \mathrm{mAh/g}$$

The theoretical capacity of tellurium is approximately 420 mAh/g. Moreover, the theoretical Capacity graphite: 372 mAh/g and Silicon: 4200 mAh/g. The lithium-ion storage reaction mechanisms of Te, Si, and graphene are as follows:

Lithium-Ion storage mechanism.

- Initial Lithiation (Discharge)

$$Te + 2Li^{+} + 2e^{-} \rightarrow Li_2Te$$

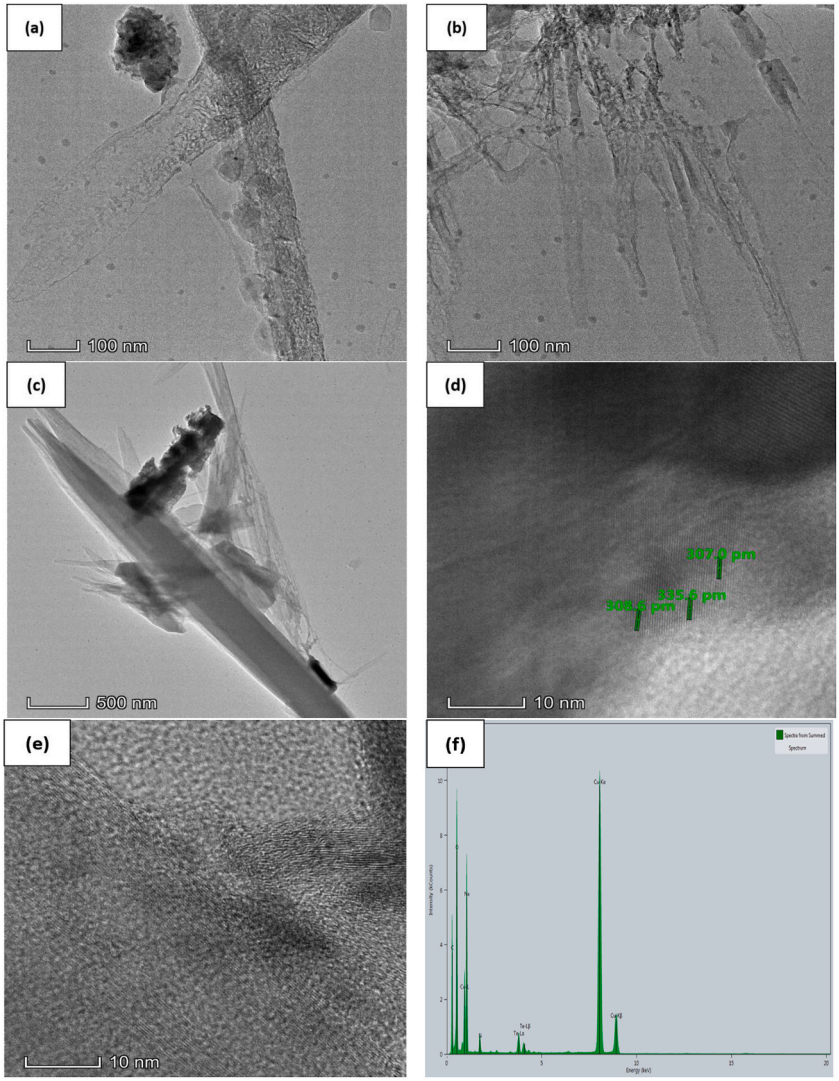

Fig. 4. Te + Gr sample (a, b, c) TEM image (d) Crystal structure with interplanar spacing (e) Crystal structure (f) EDX spectrum.

- Delithiation (charge)

$$Li_2Te \rightarrow Te + 2Li^+ + 2e^-$$

Lithium-Ion storage mechanism for Si.

- Initial Lithiation (Discharge)

$$Si + 4.4Li^+ + 4.4e^- \rightarrow Li_{15}Si_4$$

- Delithiation (charge)

$$Li_{15}Si_4 \rightarrow Si + 4.4Li^+ + 4.4e^-$$

Lithium-Ion storage mechanism for Gr.

- Initial Lithiation (Discharge)

$$6C + Li^+ + e^- \rightarrow LiC_6$$

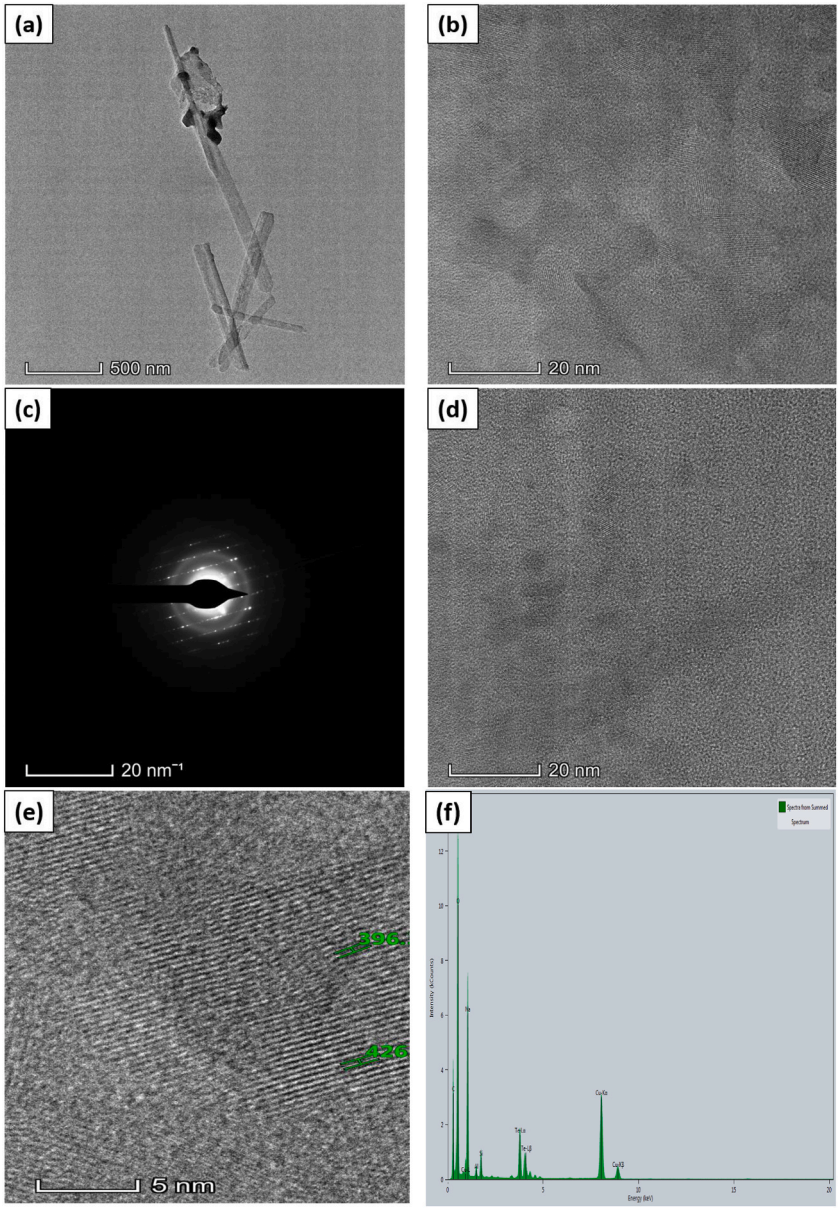

Fig. 5. Te + Si sample (a, b) TEM image (c) Electron diffraction pattern (d) Crystal structure (e) Crystal structure with interplanar spacing (f) EDX spectrum.

- Delithiation (charge)

$$LiC_6 \rightarrow 6C + Li^+ + e^-$$

3. Results and discussion

3.1. Morphological, elemental, electron, and atomic diffraction pattern analysis

A specific model of microscope operating at an accelerating voltage of 200 kV (KV) conducted the Transmission Electron Microscopy (TEM) study. For TEM testing, the samples were prepared with acetone, and these samples were sonicated for 10 min at 40 Hz in a sonicator bath. After that, samples were spread in a small quantity onto a copper grid coated with carbon. All coated samples TEM test was done before completing the CV tests.

The photos were obtained at various magnifications to achieve a full grasp of the microstructure of the samples. Figs. 3–6 are shown

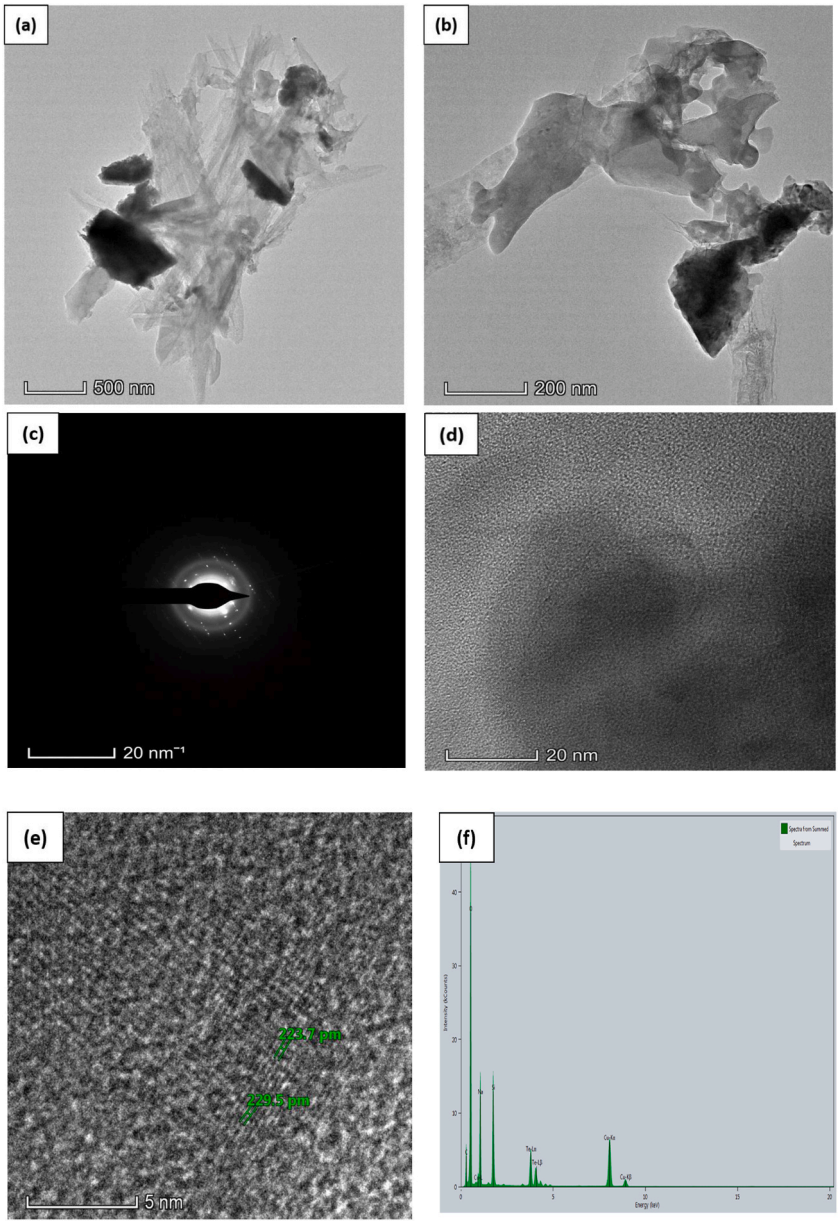

Fig. 6. Te + Si + Gr sample (a, b) TEM image (c) Electron diffraction pattern (d) Crystal structure (e) Crystal structure with interplanar spacing (f) EDX spectrum.

the TEM analysis. TEM image of the pure Tellurium (Te) specimen revealed the presence of structured interplanar space size with dimensions of 0.417 nm, 0.395 nm, and 0.443 nm. The particles exhibited a distinct and well-defined crystalline structure, occasionally aggregating into clusters. The existence of lattice fringes in the high-resolution TEM image provided proof of Tellurium's crystalline composition. The TEM picture of the Te + Gr sample made it very clear that there were particles of graphene mixed with particles of tellurium. The graphene particles were detected as thin, translucent layers around the tellurium particles, suggesting a uniform distribution. The composite structure of this sample enhances electron conductivity, mechanical stability, and interplanar space size, with readings of 0.307 nm, 0.308 nm, and 0.335 nm, respectively. These attributes are advantageous for anode materials. The Te + Si + Gr sample was examined and revealed a hierarchical structure consisting of tellurium particles contained within graphene particles, with silicon metal powder uniformly dispersed throughout the composite. The hierarchical construction results in increased electrical conductivity and mechanical strength, which in turn improves electrochemical performance. The TEM image of the Te + Si sample showed the dispersion of tellurium particles among silicon nanoparticles. The direct contact between the tellurium and silicon makes charge transfer more efficient, which improves the electrochemical properties. The sample exhibits interplanar space sizes of 0.224 nm and 0.229 nm. All samples interplanar space size are smaller than 1 nm. Using graphene and silicon metal powder enhances the

Table 2
The interplanar space size of fabricated samples.

Sample Name	The interplanar space size (pm)	The interplanar space size (nm)
Pure Te	417.1, 394.6, 442.7	0.417, 0.395, 0.443
Te + Gr	307.0, 308.6, 335.6	0.307, 0.308, 0.335
Te + Si + Gr	396.0, 426.0	0.396, 0.426
Te + Si	223.7, 229.5	0.224, 0.229

Table 3
The atomic and mass percentages of tested samples.

Sample name	Atomic number	Element	Atomic (%)	Mass (%)
Pure Te	6	C	35.58	13.28
	8	O	22.34	11.11
	11	Na	12.56	8.98
	14	Si	1.08	0.94
	29	Cu	23.65	46.70
	52	**Te**	**4.79**	**18.99**
Te + Gr	**6**	**C**	**25.70**	**9.97**
	8	O	28.02	14.48
	11	Na	15.58	11.57
	14	Si	1.29	1.17
	29	Cu	28.20	57.87
	52	**Te**	**1.20**	**4.94**
Te + Si + Gr	**6**	**C**	**23.86**	**11.45**
	8	O	41.88	26.77
	11	Na	18.28	16.78
	13	Al	0.86	0.93
	14	**Si**	**2.14**	**2.41**
	29	Cu	9.55	24.25
	52	**Te**	**3.42**	**17.43**
Te + Si	6	C	11.09	5.39
	8	O	54.10	35.03
	11	Na	12.95	12.05
	14	**Si**	**11.83**	**13.45**
	29	Cu	6.82	17.53
	52	**Te**	**3.21**	**16.56**

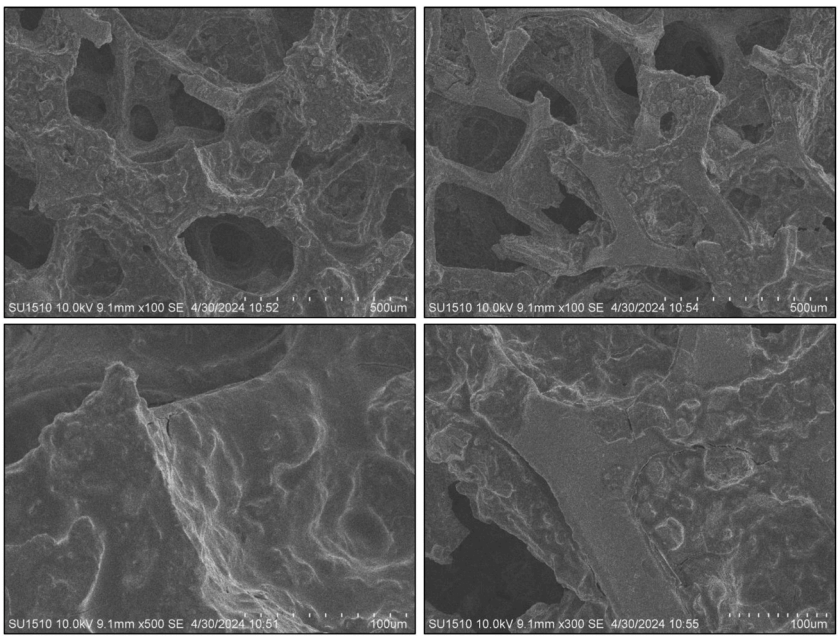

Fig. 7. Sem spectroscopy of the pure Te sample coated on nickel foam.

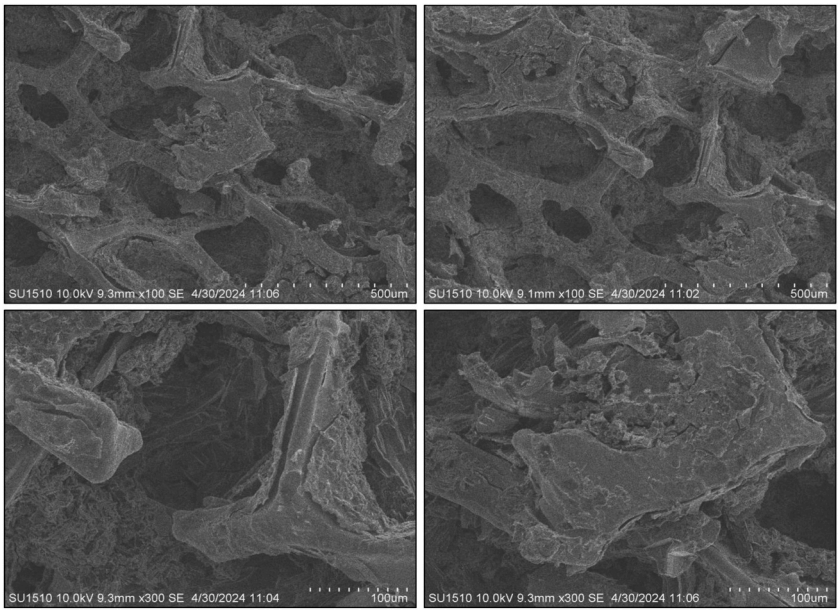

Fig. 8. Sem spectroscopy of the Te + Gr sample coated on nickel foam.

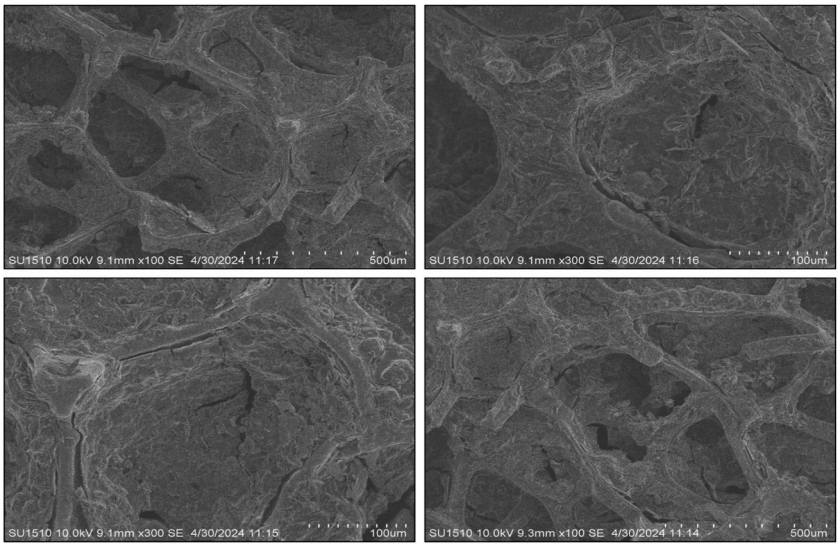

Fig. 9. Sem spectroscopy of the Te + Si + Gr sample coated on nickel foam.

samples surface structure, leading to enhanced charge transfer and improved electrochemical properties. The TEM images for these samples have scales of 200 nm, 500 nm, 20 nm, and 5 nm. Table 2 the interplanar space size of anode samples and Table 3 gives the elemental atomic and mass percentages of all anode samples. The detected elements, including O, Na, Al, and Cu, are impurities introduced during sample preparation or from the materials used (like the acetone or copper grid).

3.2. Microstructural surface analysis after charging-discharging process

SEM analysis was used to examine the microstructure of composite anode films. All coated sample morphology was done after completing the CV tests. The pure Te sample exhibits a volume change during the charging and discharging cycle, highlighting a significant issue with tellurium as a battery material that impacts battery performance. To overcome this issue, other samples were composited with graphene (wt%) and silicon (wt%). The morphological image reveals that the addition of these materials reduces the volume expansion of the Te + Gr, Te + Si + Gr, and Te + Si samples, respectively. However, it have some cracks, These cracks typically appeared during the preparation of samples for SEM testing. which can also affect battery performance. Figs. 7–10 show the SEM

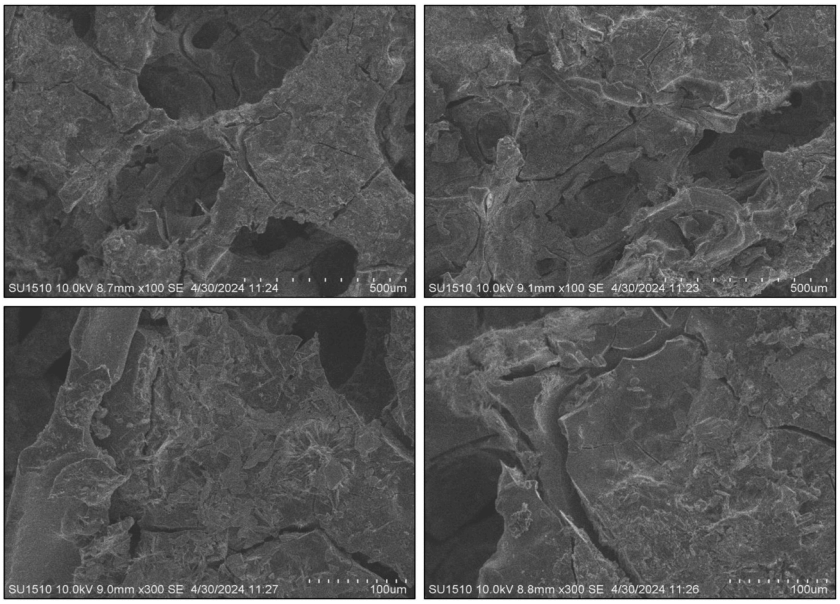

Fig. 10. Sem spectroscopy of the Te + Si sample coated on nickel foam.

spectroscopy of four samples with different scales (500 μm, 100 μm) under 10 KV. The overall outcome of this test demonstrates that surface structure and particle dispersion have a potential impact on the battery anode materials.

3.3. Chemical states and elemental Evaluation using XPS analysis

The XPS survey scan showed that tellurium (Te) was the main element in all of the samples, which matches the make-up of the tellurium-based anode material. XPS spectra are used to analyze the chemical states of tellurium and another element within the anode material. The spectrum revealed distinct peaks corresponding to different element compositions present in the material [30]. Figs. 11–14 show the XPS and narrow spectroscopy of the tested samples.

The XPS spectrum of the pure Te sample exhibits two distinct peaks: elemental Tellurium (TeO) and Tellurium oxides (TeOx). In the pure Te sample, the elemental peaks are 572.0 eV (Te 3d5/2) and 582.0 eV (Te 3d3/2), and the oxides peak at 580.0 eV. Additionally, detected traces of oxygen (O) and carbon (C) peaks, which originate from surface oxidation and contamination. In the 2nd sample (Te + Gr), the elemental and oxide peaks of tellurium are the same as in the pure Te sample. In this sample, the graphene elemental and oxide peaks are 284.0 eV (C-C/C=C) and 286.0 eV (C-O). The elemental and oxide peaks observed in the Te + Si + Gr sample are 99.0 eV (Si 2p3/2), 103.0 eV (Si 2p1/2) for elemental peaks, and 103.0 eV for oxide peaks. The sample's silicon peaks display noise. However, the tellurium and graphene peak values are similar to the Te + Gr sample. The sample combines with tellurium and silicon in the Te + Si sample, there the elemental and oxide peaks of the tellurium and silicon values in this sample are similar to those of the Te + Si + Gr sample. Additionally, the silicon peaks in this sample exhibit greater stability compared to the Te + Si + Gr sample. Table 4 represents the elemental and oxide peaks of tested samples. Table 5 shows the atomic percentage of all materials from XPS spectroscopy. This percentage shows that all samples are oxidized due to higher oxidation sensitivity of tellurium and graphene [31]. In battery materials, higher oxidation levels lead to a decrease in their performance and this is one of the limitations of this study. Moreover, The element Na was also detected in the samples; it was an impurity introduced during sample preparation before testing.

3.4. Crystallographic analysis of fabricated materials using XRD

The X-ray diffraction (XRD) [32] analysis aims to understand the crystal structure and phase composition of Tellurium-base composite anode materials made of pure Te samples, Te + Gr, Te + Si + Gr, and Te + Si. This analysis is crucial for optimizing its electrochemical performance. The XRD analysis was performed using Cu Kα radiation (λ = 1.5406 Å) at room temperature.

Fig. 15 shows all XRD spectroscopy of anode samples of pure Te, Te + Gr, Te + Si + Gr, and Te + Si, and the scanning range was from 10° to 80° (2θ). The diffraction peaks seen in the Pure Te sample were at 2θ (Te) = 23.13°, 27.67°, 38.39°, 40.65°, 43.55°, 46.04°, 47.28°, 49.88°, 51.47°, 57.15°, 63.06°, 64.07°, 66.22°, 68.12°, 72.46°, 73.95°, and 75.97°. These points correspond to the crystallographic (hkl) planes (100), (101), (102), (110), (111), (003), (200), (201), (112), (022), (113), (210), (121), (023), (212), (300), and (301). The second sample (Te + Gr) combines tellurium powder with graphene 2D materials. The peak observation of this sample was at 2θ (Te) = 23.09°, 27.63°, 38.36°, 40.56°, 43.47°, 49.78°, 51.39°, 57.06°, 62.98°, 66.09°, 67.86°, 72.38°, 75.81°, and 2θ (Gr) = 26.54°, 43.54°, 46.39°, 54.65°, 63.65°, 77.89°. The tellurium peaks and crystallographic planes of this sample remained the same as in the pure Te sample and Graphene: (003), (101), (012), (006), (104), (015), and (110). The highest point of the Te + Si + Gr composite

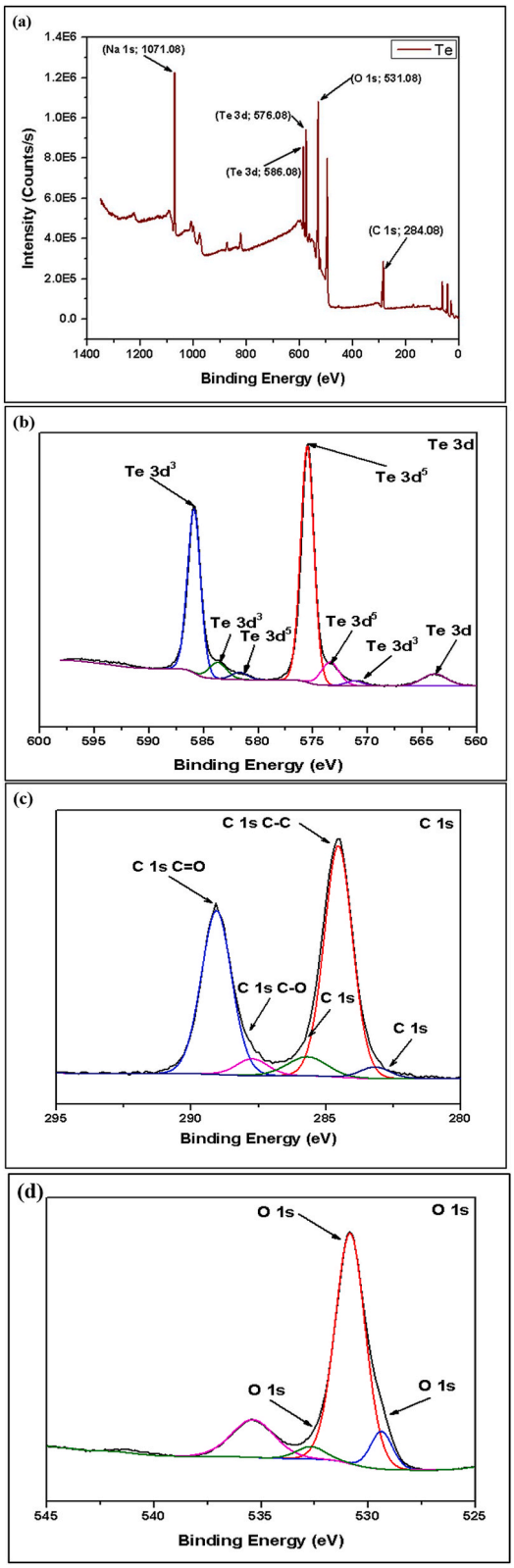

Fig. 11. Pure Te (a) XPS Spectroscopy of Pure Te Sample, (b, c, d) Narrow Spectroscopy of Te 3d, C 1s, and O 1s.

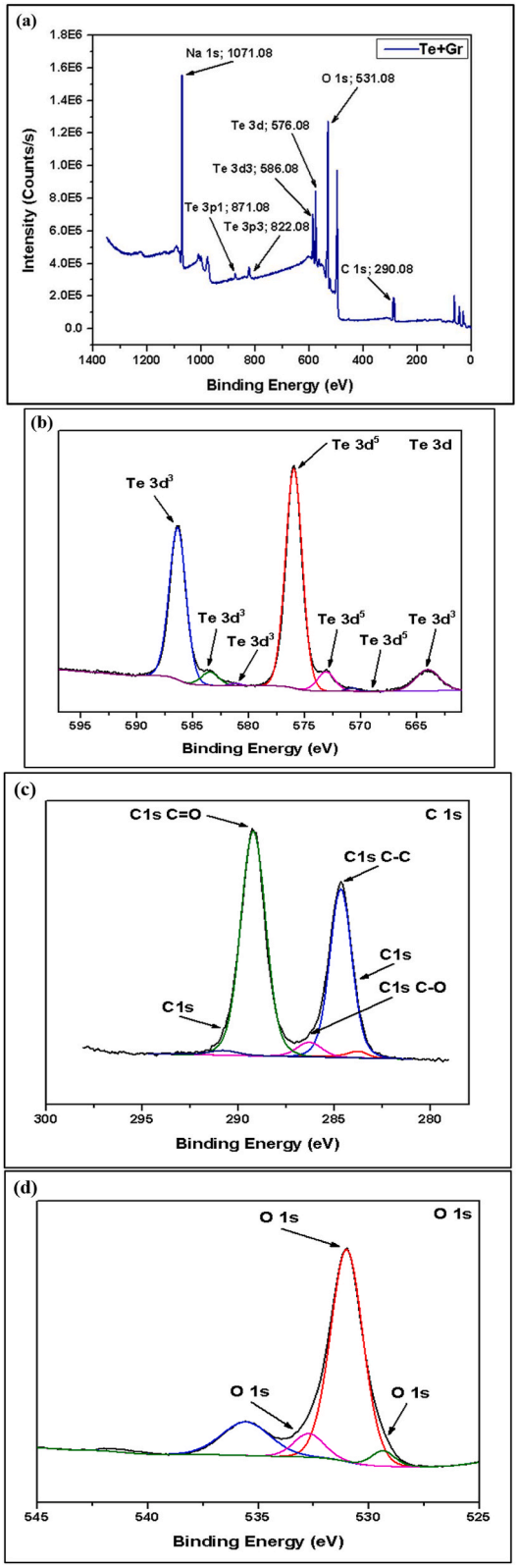

Fig. 12. (a) XPS Spectroscopy of Te + Gr Sample, (b, c, d) Narrow Spectroscopy of Te 3d, C 1s and O 1s.

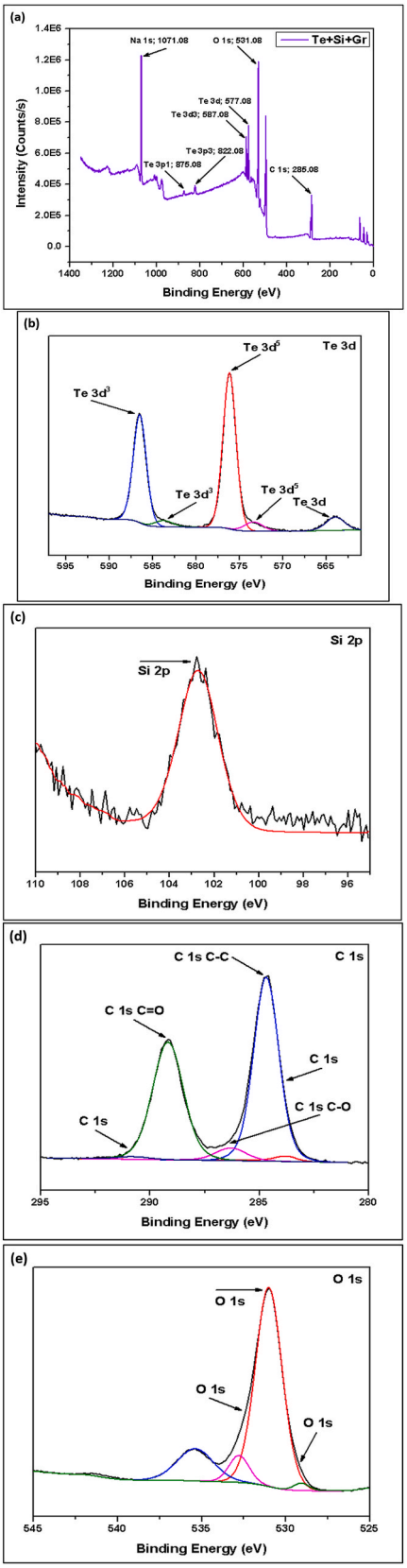

(caption on next page)

Fig. 13. (a) XPS Spectroscopy of Te + Si + Gr Sample, (b, c, d, e) Narrow Spectroscopy of Te 3d, Si 2p, C 1s and O 1s.

sample was seen at 2θ, (Gr) = 26.58°, 41.91°, 44.13°, 50.32°, 54.75°, 59.58°, 71.26°, and 76.56°, which are (002), (100), (101), (102), (004), (103), (104), and (110). Silicon peaks and the crystallographic planes are 2θ (Si) = 28.53°, 47.14°, 56.29°, 59.04°, 69.37°, 76.64° and (111), (220), (222), (400), and (331). The tellurium peaks and crystallographic planes in this sample are nearly identical. However, The Te + Si sample exhibits a composite of tellurium and silicon. The XRD peak positions and crystallographic planes for tellurium (Te) and silicon (Si) remained stable, as in the above samples.

The degree of crystallinity is calculated by using the formula mentioned below.

i. The degree of crystallinity (%),

$$\mathbf{X_C} = \frac{\boldsymbol{A_c}}{(\boldsymbol{A_c} + \boldsymbol{A_a})} \tag{1}$$

where, A_c = Crystalline areaA_a = Amorphous area.

And, the Crystallites Size (nm) is calculated by using the Scherrer equation, Dislocation density, and Microstrin mentioned below.

ii .

$$\mathbf{D} = \frac{\boldsymbol{K\lambda}}{\boldsymbol{\beta}\,\mathbf{cos}\,\boldsymbol{\theta}} \tag{2}$$

where, K = 0.9 (Scherrer constant)λ = 0.154006 nm (Wavelength of the X-ray source)β = FWHM (Full width at half maximum) in radiansθ = Peak position (radians)

iii. **Dislocation density**,

$$\boldsymbol{\delta} = \mathbf{1}/\boldsymbol{D^2} \tag{3}$$

where, D = Crystallites size (nm)

iv. **Microstrain,**

$$\boldsymbol{\varepsilon} = \boldsymbol{\beta}/\mathbf{4}\,\mathbf{tan}\,\boldsymbol{\theta} \tag{4}$$

where, β = FWHM (radians)θ = Peak Position (radians)

Table 6 illustrates the values of the percentage of crystallinity, average crystallite grain Size, dislocation density, and average microstrain (ε) from XRD spectroscopy. Increased crystallinity typically signifies improved structural organization and conductivity, while the average size of crystalline grains influences mechanical strength and charge transport properties [33]. Dislocation density reflects imperfections in the crystal lattice that can impact mechanical properties and ion diffusion [34], and microstrain quantifies the distortion or strain within the crystal lattice. Elevated microstrain values can have a significant effect on the stability of materials and their electrochemical performance [35].

Fig. 16 shows the relation among the average crystallite grain size, dislocation density, and average microstrain of all samples. In this figure, it is shown that the pure Te, Te + Si + Gr and Te + Si samples exhibit significant crystallinity, with values of 53.39 %, 54.19 %, and 51.14 % respectively, indicating a well-organized crystalline phase. This promotes efficient charge transfer and enhances the durability of battery electrodes. The grain sizes of tested samples, which vary from around 33.98 nm–39.62 nm, are within an acceptable range for battery materials. This suggests that the samples have the potential to exhibit favorable conductivity and stability. Nevertheless, the dislocation densities of these samples are comparatively low, varying from 0.00064 nm^{-2} to 0.00086 nm^{-2}. This characteristic is beneficial as it helps to preserve the structural integrity and electrical conductivity of battery electrodes. The microstrain values vary from 0.153 to 0.424, the higher values suggest that there may be difficulties in maintaining stability and performance during cycling conditions.

3.5. Thermal stability analysis using TGA and DSC methods

Fig. 17 illustrates the results of Thermogravimetric analysis (TGA) and Differential Scanning Calorimetry (DSC) conducted on samples of pure Te, Te + Gr, Te + Si + Gr, and Te + Si. Thermogravimetric analysis was conducted under ambient atmospheric conditions. The subsequent observations were recorded for the uncontaminated pure Te sample: A modest weight reduction (5.21 %) occurs at temperatures below 200 °C, with the sample's initial temperature being 93.79 °C. The initial temperatures at which the samples Te + Gr, Te + Si + Gr, and Te + Si start to experience weight loss are 70.24 °C, 72.24 °C, and 84.02 °C, respectively. This weight loss corresponds to 7.17 %, 7.03 %, and 7.79 % of the total weight. The following phase of this analysis reveals the onset temperatures of these samples to be 561.90 °C, 542.34 °C, 593.00 °C, and 530.56 °C, respectively. The weight reductions of the Pure Te, Te + Gr, Te + Si + Gr, and Te + Si samples are 73.58 %, 46.27 %, 38.61 %, and 36.64 %, respectively. The TGA analysis indicates

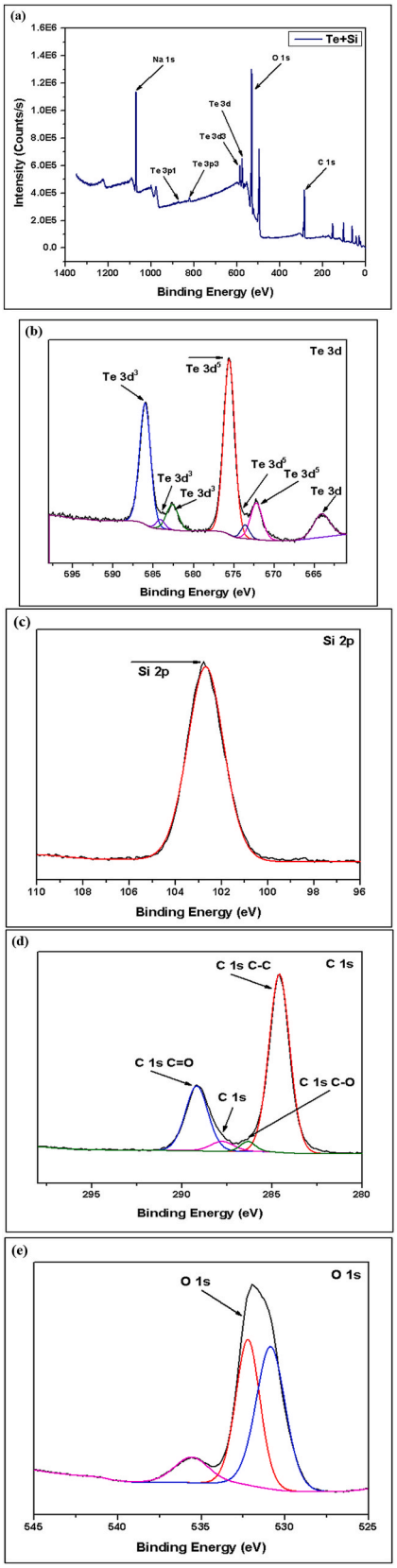

(caption on next page)

Fig. 14. (a) XPS Spectroscopy of Te + Si Sample, (b, c, d, e) Narrow Spectroscopy of Te 3d, Si 2p, C 1s and O 1s.

Table 4
It represents the elemental and oxide peaks of tested samples.

Sample Name	Elemental Peaks	Oxides Peaks
Pure Te	572.0 eV (Te 3d5/2) and 582.0 eV (Te 3d3/2)	Te 3d peaks, 580.0 eV
Te + Gr	284.0 eV (C-C/C=C)	286.0 eV (C-O)
Te + Si + Gr	99.0 eV (Si 2p3/2) and 103.0 eV (Si 2p1/2)	Si 2p peaks, 103.0 eV for SiO_2
Te + Si	99.0 eV (Si 2p3/2) and 103.0 eV (Si 2p1/2)	Si 2p peaks, 103.0 eV for SiO_2

Table 5
The atomic percentage of tested materials from XPS spectroscopy.

Atomic (%)	Sample name			
	Pure Te	Te + Gr	Te + Si + Gr	Te + Si
C 1s	37.18	27.13	37.05	33.23
O 1s	41.75	46.43	44.54	43.48
Te 3d	3.36	2.43	1.92	0.94
Si 2p	-	-	1.23	10.99
Na1s	17.71	23.18	15.27	11.36

that the samples Te + Si + Gr and Te + Si exhibit greater thermal stability compared to the samples pure Te and Te + Gr. In addition, the sample Te + Si + Gr shows an extra decrease in weight at around 700.00 °C, with a weight loss of 8.91 % and a starting temperature of 700.82 °C, respectively. Table 7 provides a thorough examination of the percentage of weight reduction at various temperatures.

The DSC quantifies the heat flow into or out of a sample to temperature or time. Every sample underwent the following observations: The pure Te sample undergoes several phase transitions, including a glass transition occurring at a temperature of 77.50 °C, endothermic peaks at 109.36 °C, and documented melting peaks at 553.00 °C. The Te + Gr sample undergoes a glass transition at a temperature of 76.50 °C, exhibits endothermic peaks at 113.36 °C, and displays melting peaks at 450.00 °C. Furthermore, the Te + Si + Gr and Te + Si samples experience a glass transition at temperatures of 69.00 °C and 75.00 °C, respectively. Furthermore, they demonstrate endothermic peaks at temperatures of 99.58 °C and 117.14 °C, as well as melting peaks at temperatures of 449.50 °C and 450.50 °C, respectively. All TGA and DSC spectroscopy of these samples are illustrated in Fig. 18. Tellurium is a semiconductor that can exist in several crystalline forms, known as polymorphs, depending on the temperature. At room temperature, the most stable form of

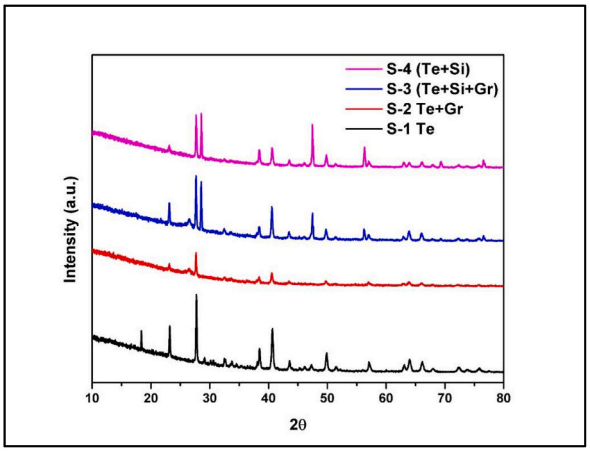

Fig. 15. Xrd spectroscopy of anode samples.

Table 6
Percentage of crystallinity average, crystallites grain size, dislocation density, and avetage microstrain of anode samples.

No. of Sample	% of Crystallinity	Average Crystallites Grain Size (nm)	Dislocation density (nm^{-2})*1000	Average Microstrain (ε)
S1 (Pure Te)	53.39	35.66	0.786251	0.153
S2 (Te + Gr)	34.76	33.98	0.86568	0.224
S3 (Te + Si + Gr)	54.19	38.03	0.691516	0.424
S4 (Te + Si)	51.14	39.62	0.636904	0.318

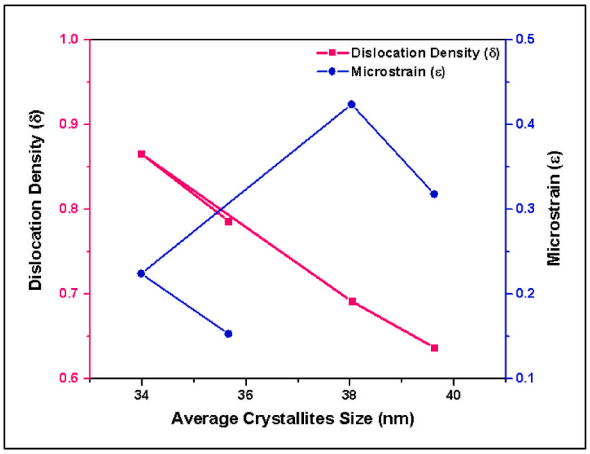

Fig. 16. Relation among the average crystallite grain size, dislocation density, and average microstrain of anode samples.

tellurium is rhombohedral (α-Te) [36]. However, at higher temperatures, it transforms into a less stable and denser form known as β-Te [37,38]. A higher melting peak area observed in the differential scanning calorimetry (DSC) analysis of pure Tellurium material suggests a reduced level of thermal stability. Tellurium composites including silicon (wt%) and graphene (wt%) reduce the size of the melting peak area. Te + Gr, Te + Si + Gr, and Te + Si samples have greater thermal stability than pure Te samples at elevated temperatures. The Te + Si + Gr sample exhibits the most significant degree of thermal stability among all the samples.

3.6. Absorbance range analysis of level of stability using UV

The limited absorbance range suggests that the battery materials exhibit a high level of stability when exposed to UV radiation [39]. Materials with high UV light absorption tend to deteriorate when exposed to UV radiation, resulting in decreased battery performance or lifespan. Fig. 19 displays the UV-spectroscopy results for all samples in this test that have a low absorbance range, indicating that they are suitable for battery materials.

3.7. Cyclic volummetry analysis

The performance of the battery samples is determined by the specific capacitance (C) values acquired from cyclic voltammetry (CV) testing at different scan rates. The specific capacitance is a crucial statistic for evaluating battery performance since it directly measures the charge storage capacity of the electrode material [40,41]. The electrochemical techniques such as cyclic voltammetry were performed on a coated nickel foam in a 3.5 % NaCl as a solution. Electrochemical measurements were performed in the potential range of −1.0 to 1.0 V with a scan rate of 25 mV/s, 50 mV/s, and 100 mV/s. Basi Epsilon Electrochemical Workstation with C-3 electrochemical cell was used to perform the test. Where copper and platinum plates with an area of 1.0 cm^2 constituted the working and auxiliary electrodes, using the Ag/AgCl electrode as a reference. (BCSIR)

Figs. 20–23 the cyclic voltammetry (CV) analysis of all tested at different scan rates. The pure Te sample exhibits a decline in specific capacity values across all scan rates, indicating a deterioration in charge storage capacity across successive cycles. As the scanning rates increase, the specific capacity values fall, suggesting constraints in charge transfer and electrode kinetics. The specific capacitance is calculated from Equation (5) by the concept of Fig. 24. In addition, the specific capacitance is converted into the specific capacity using Equation (6). The decrease in Cp values seen at higher scan rates (100 mV/s) indicates that the charge storage and electrode kinetics are constrained when the cycling occurs at a faster pace. When the Te + Gr sample demonstrates significant specific capacity values, suggesting excellent charge storage capacity. Nevertheless, the specific capacity values exhibit a substantial reduction during cycling, particularly at higher scan rates, indicating constraints in charge retention and stability. The Te + Si + Gr sample in its pure form demonstrates superior specific capacity values at lower scan rates (25 mV/s and 50 mV/s), suggesting enhanced charge storage capacity.At reduced scan rates, the Te + Si sample is cycled, and there is an observed increase in specific capacity values, suggesting an enhancement in charge storage performance. Nevertheless, when the scan rates are increased to 50 mV/s and 100 mV/s, the specific capacity values exhibit a substantial drop, indicating constraints in the kinetics of charge transfer. In general, samples that exhibit consistent and high specific capacity values at lower scan speeds indicate excellent ability to store and maintain charge. Decreasing Cp values with increasing scan rates indicate that the speed of cycling limits the charge transfer kinetics and electrode performance and Fig. 25 show the graph specific capacity (Cp) versus cycles at different scan rate. Table 8 The specific capacity and charge (Q/m) values when sodium chloride (NaCl) was used as the electrolyte.

i. **Calculation of Specific Capacitance (C):**

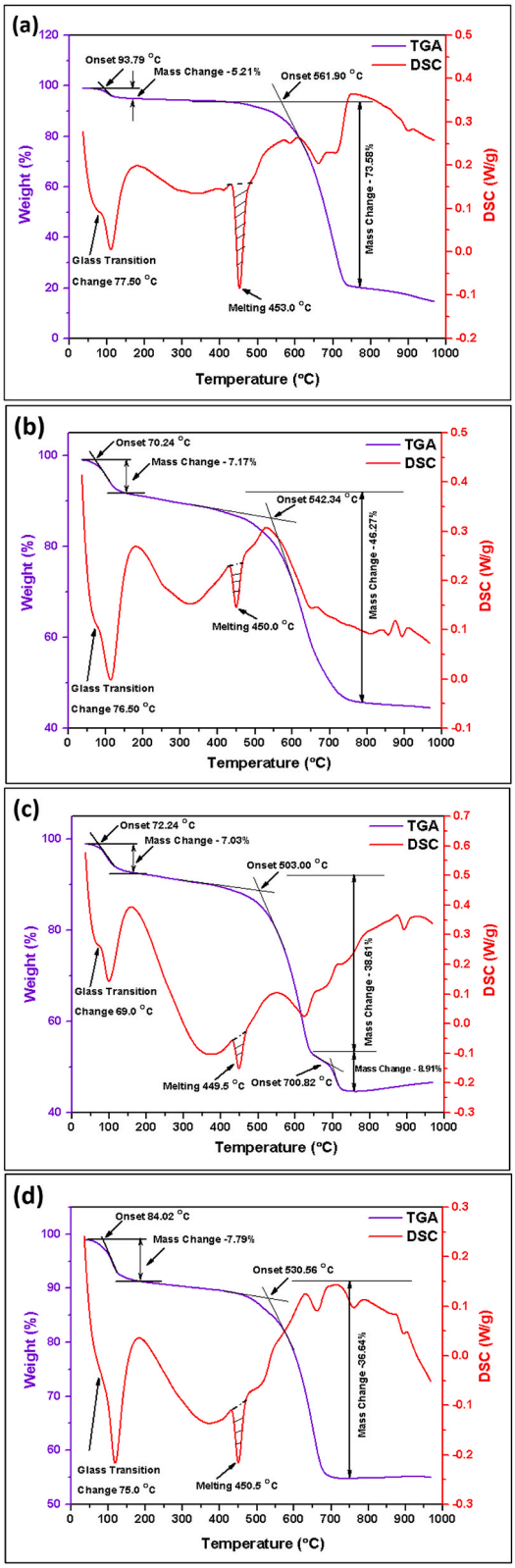

Fig. 17. TGA and DSC Analysis of Samples (a) pure Te, (b) Te + Gr, (c) Te + Si + Gr, and (d) Te + Si.

Table 7
Percentage of weight losses at various temperatures for all tested samples.

Samples Name	Weight Losses (%)								
	100 °C (W_{100})	200 °C (W_{200})	300 °C (W_{300})	400 °C (W_{400})	500 °C (W_{500})	600 °C (W_{600})	700 °C (W_{700})	800 °C (W_{800})	900 °C (W_{800})
Pure Te	2.65	2.38	0.54	0.50	2.41	9.53	43.65	18.54	2.37
Te + Gr	4.20	4.68	1.73	1.40	3.45	12.51	21.89	4.53	0.78
Te + Si + Gr	4.78	3.04	1.34	1.18	3.71	18.86	18.03	3.86	0.84
Te + Si	3.68	5.20	0.73	0.86	2.02	9.53	22.80	0.15	0.15

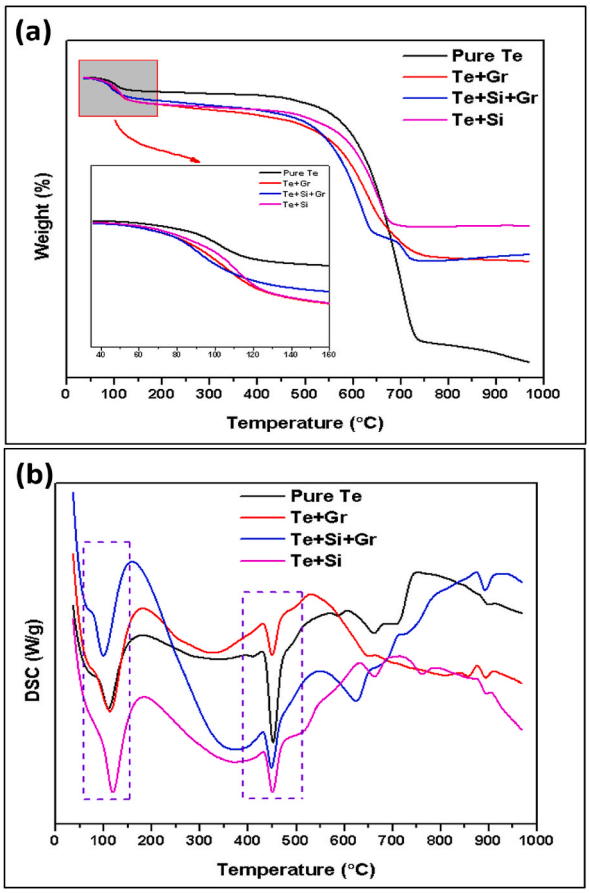

Fig. 18. (a, b) All TGA and DSC Spectroscopy of Tested Samples.

$$C = \frac{A}{2mk(V2 - V1)} \quad (5)$$

Scan rate = k (mV/s)
Mass of the coated material = m (g)
Potential window Δ V= (V_2-V_1)
The area inside the CV curve = A.
Specific Capacitance = C (F/g)

ii. **Specific Capacity (Cp):**

$$\text{Specific Capacity } (mAh/g) = \text{Specific Capacitance } (F/g) \times \text{Voltage} \times 3600 \quad (6)$$

iii. **Charge (Q/mass):**

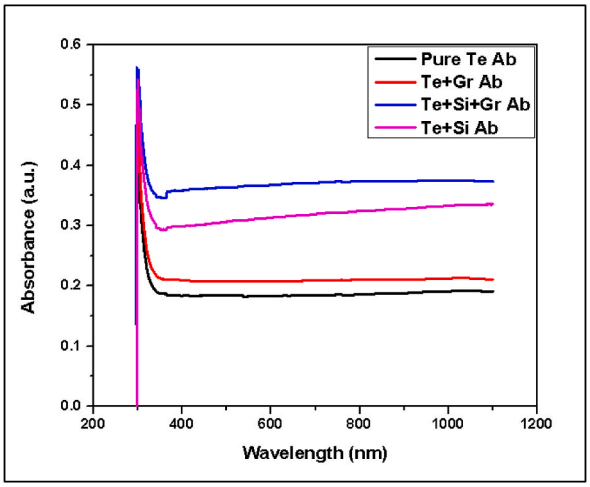

Fig. 19. All tested samples UV spectroscopy.

$$\text{Charge (Q / mass) (C / g)} = (\text{Specific Capacitance (C)} \times \text{Mass of the active material}) \quad (7)$$

Fig. 25 illustrates the specific capacity as a function of the number of cycles at scan rates of 25, 50, and 10 mV/s.

3.8. Electrochemical impedance spectroscopy (EIS) analysis

Following a 21-day immersion period (equivalent to 3 weeks), the samples were analyzed using electrochemical impedance spectroscopy (EIS). The EIS measurement was conducted utilizing a 3.5 wt% aqueous solution of sodium chloride (NaCl) as the electrolyte. The equivalent series resistance (R_S) denotes the cumulative internal resistance of the battery, encompassing electrode, electrolyte, and interfacial resistances. Lower values of R_S indicate decreased resistance in the battery system, resulting in enhanced energy efficiency and diminished power losses during charge and discharge cycles [42,43]. The values of the electrochemical impedance spectroscopy (EIS) for the different samples are as follows: 29.99 Ω for the pure Te sample, 28.13 Ω for the Te + Gr sample, 30.53 Ω for the Te + Si + Gr sample, and 44.05 Ω for the Te + Si sample. The Te + Gr and Te + Si + Gr samples have relatively lower levels of electrical resistance (R_S) ranging from 28 to 31 Ω. This indicates that these samples have lower internal resistance and higher overall conductivity compared to pure Te and Te + Si samples.

The charge transfer resistance (R_{ct}) is a measure of the resistance at the interface between the electrode and the electrolyte. It affects the speed at which charge transfer processes, such as ion diffusion and electron transfer, occur. Lower R_{ct} values indicate faster charge transfer kinetics and better electrode performance [44,45]. The next part of the spectrum is the semicircle (a-b), which spans from the high to the mid-frequency region. This section is known as the charge transfer resistance (R_{ct}). The diameter values for the pure Te sample, Te + Gr sample, Te + Si + Gr sample, and Te + Si sample are 759.07 Ω, 4.21 Ω, 36.39 Ω, and 164.905 Ω, respectively. The Te + Gr sample has the most favorable charge transfer efficiency at the electrode contact, as evidenced by its lowest R_{ct} value of 4.21 Ω. The Te + Si + Gr sample also demonstrates a comparatively low R_{ct} value of 36.39 Ω, indicating favorable charge transfer kinetics. The R_{ct} values of pure Te and Te + Si samples are greater, measuring 759.07 Ω and 164.905 Ω, respectively. This suggests that there may be difficulties in achieving efficient charge transfer and kinetics, Table 9 gives the equivalent series resistance (R_S) and the charge transfer resistance (R_{ct}) of all samples. Fig. 26 shows the EIS data of electrodes (a) Pure Te (b) Te + Gr (c) Te + Si + Gr and (d) Te + Si.

The charge transfer resistance (R_{ct}) calculation formula.

iv. The charge transfer resistance (R_{ct}) = Maximum internal resistance (R_b) - The equivalent series resistance (R_S) ….(4.8)

The phase angle quantifies the time delay between the applied voltage and the resultant current in an AC impedance test. It illustrates the correlation between the resistive (real) and capacitive (imaginary) elements of impedance. Lower phase angles indicate greater resistance, whereas higher phase angles suggest increased capacitance. The pure Te sample demonstrates a reduced phase angle (1.47), which can be advantageous for the use of simpler and more resistive electrode materials. The Te + Si sample exhibits a moderate phase angle of 11.04, indicating a balanced combination of resistive and capacitive behavior that is appropriate for standard battery electrodes. On the other hand, the Te + Gr and Te + Si + Gr samples display higher phase angles of 54.69 and 37.73, respectively, suggesting a greater emphasis on capacitive behavior. This makes them potentially suitable for high-capacity electrodes, which could be advantageous for materials used in high-energy-density batteries. Fig. 27 shows the electrochemical impedance spectroscopy (EIS) curves: (a) Nyquist plot and (b) phase angle.

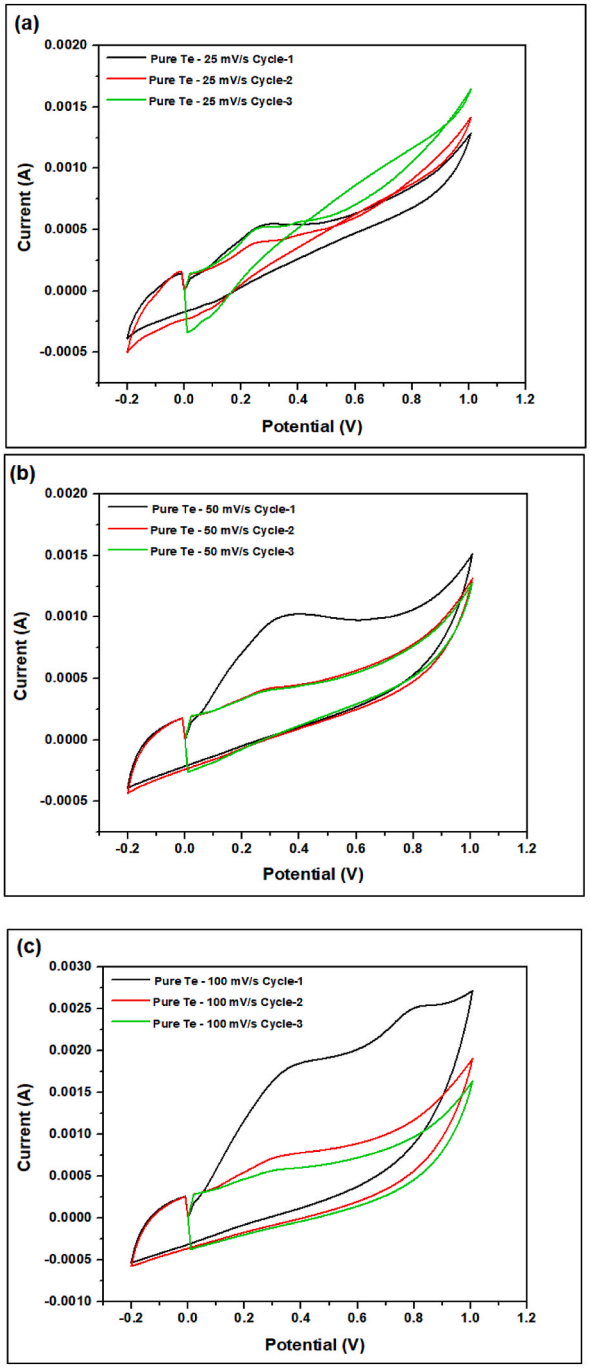

Fig. 20. The cyclic voltammetry (CV) analysis of pure Te sample at different scan rates (a) 25 mV/s (b) 50 mV/s (c) 100 mV/s.

3.9. The advantages of this work compared with previous literatures

Table 10.

4. Conclusions

In summary, tellurium combined with graphene and silicon are found to be promising anode materials in this work for energy storage applications due to their better specific capacity (Cp) and low charge transfer resistance (R_{ct}). In addition, the fabricated anode materials have better physical and thermal stability due to their chemical integrity. Hopefully, in the future, the results obtained from

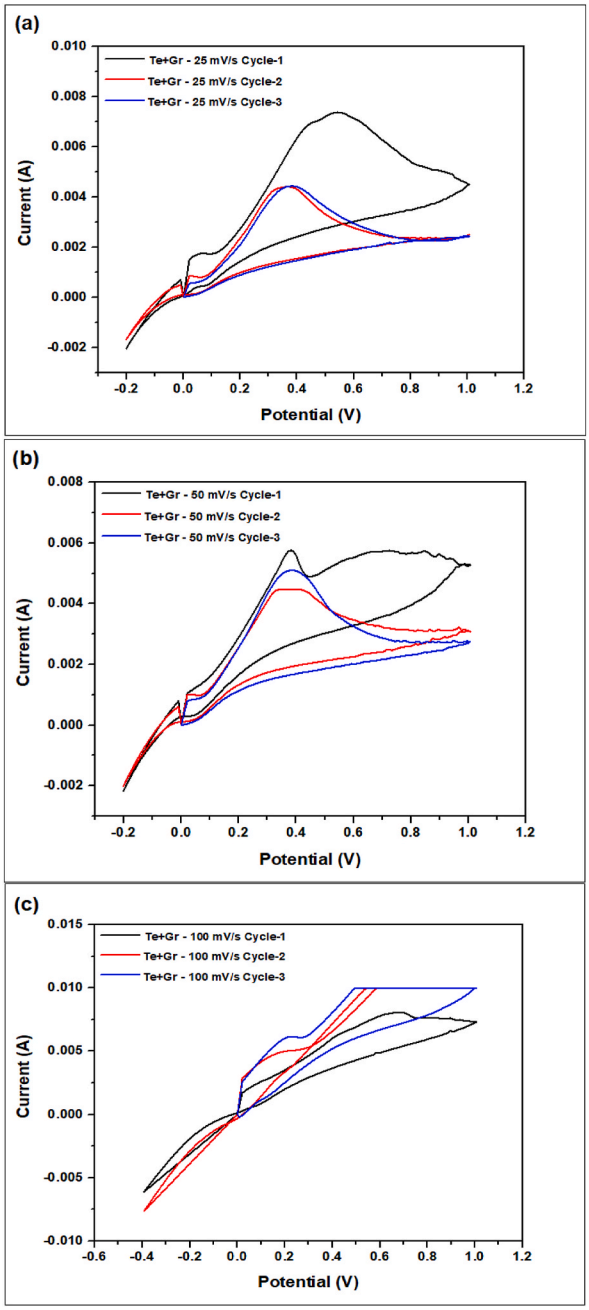

Fig. 21. The cyclic voltammetry (CV) analysis of the Te + Gr sample at different scan rates (a) 25 mV/s (b) 50 mV/s (c) 100 mV/s.

this work can be used as reliable sources for further research and commercial applications of tellurium composite films as anode in industry.

The details conclusions from this study can be drawn as follows.

I. The TEM images of pure Tellurium specimens show interplanar spaces measuring 0.417 nm, 0.395 nm, and 0.443 nm. For the Te + Gr sample, the interplanar spaces measure 0.307 nm, 0.308 nm, and 0.335 nm. For the Te + Si + Gr sample, the interplanar spaces measure 0.396 nm, 0.424 nm. Lastly, for the Te + Si sample, the interplanar spaces measure 0.224 nm and 0.229 nm. All interplanar spaces in the samples have sizes smaller than 1 nm. Graphene and silicon metal powder improve the surface morphology of tellurium.

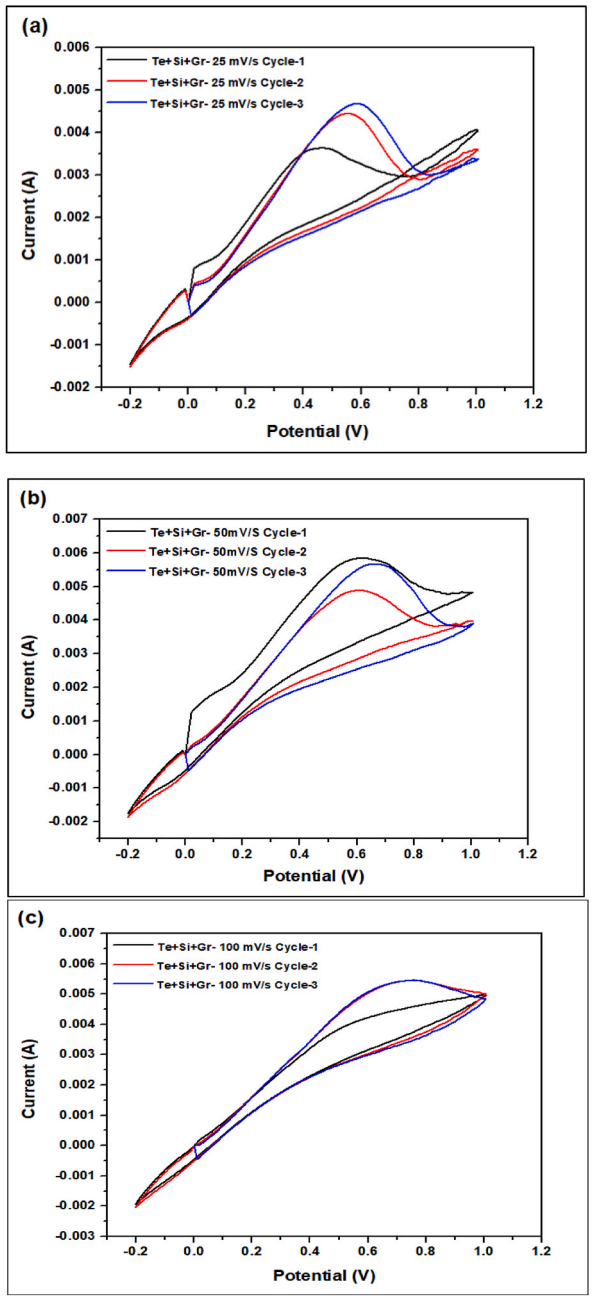

Fig. 22. The cyclic voltammetry (CV) analysis of the Te + Si + Gr sample at different scan rates (a) 25 mV/s (b) 50 mV/s (c) 100 mV/s.

II. An SEM study after the CV test reveals that pure tellurium changes volume during charging and discharging, impacting battery performance. Combining graphene and silicon reduced volume growth in Te + Gr, Te + Si + Gr, and Te + Si samples, but fractures could negatively affect battery functioning.

III. The XPS spectrum of pure Tellurium (Te) shows two distinct peaks: elemental Tellurium (TeO) and Tellurium oxides (TeOx). The pure Te sample has peaks at 572.0 eV and 582.0 eV, while the oxides peak is at 580.0 eV. The second sample (Te + Gr) has identical peaks, while the Te + Si + Gr sample has identical elemental peaks and an oxide peak. The silicon peaks exhibit noise in the Te + Si + Gr sample, but the tellurium and graphene values are comparable. The presence of oxides could affect the samples electrochemical performance in lithium-ion battery applications.

IV. XRD analysis reveals material structural characteristics like crystallinity, grain size, dislocation density, and microstrain. Samples show variations in these characteristics, impacting structural quality. Increased crystallinity and larger grain sizes

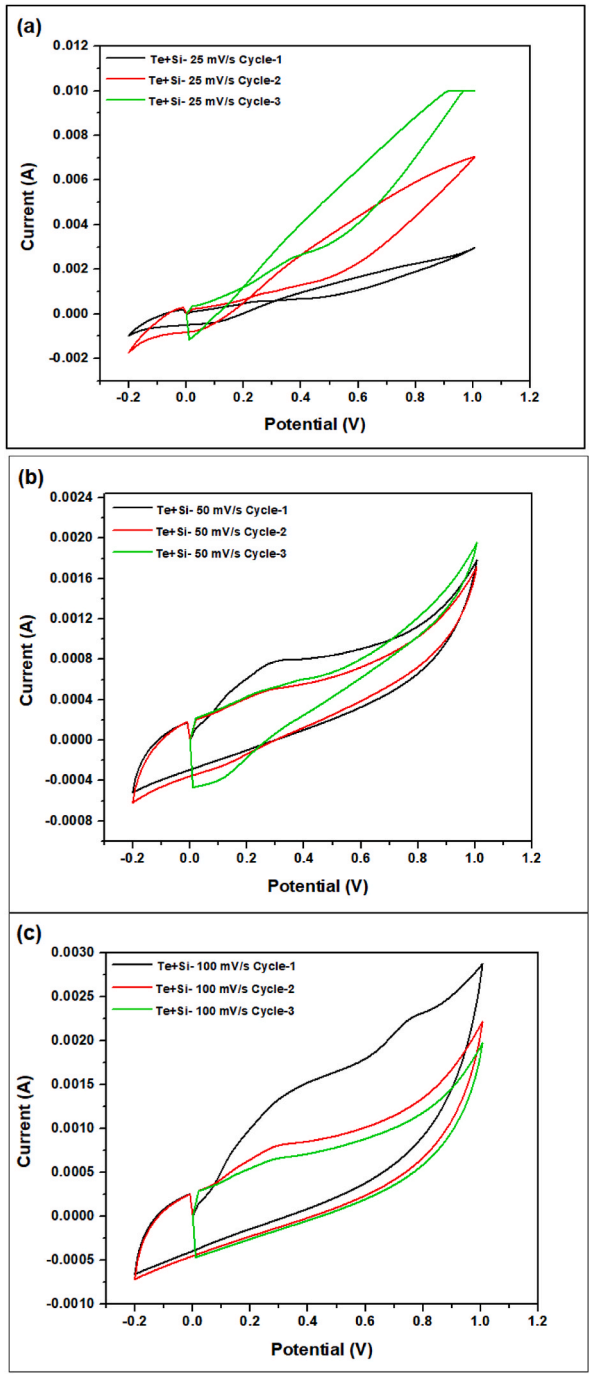

Fig. 23. The cyclic voltammetry (CV) analysis of the Te + Si sample at different scan rates (a) 25 mV/s (b) 50 mV/s (c) 100 mV/s.

indicate better conductivity and mechanical stability, beneficial for battery electrodes. XRD data also influence battery performance, including charge/discharge behavior, cycle life, and capacity retention.

V. TGA analysis reveals that Te + Si + Gr and Te + Si samples show higher thermal stability compared to Pure Te and Te + Gr samples. The melting peak region found in the DSC examination of pure tellurium material indicates a decreased level of thermal stability. Tellurium composites including silicon (wt%) and graphene (wt%) decrease the size of the melting peak region. The thermal stability of Te + Gr, Te + Si + Gr, and Te + Si samples is higher than that of pure Te samples at high temperatures. The Te + Si + Gr sample demonstrates the highest level of thermal stability compared to all other samples.

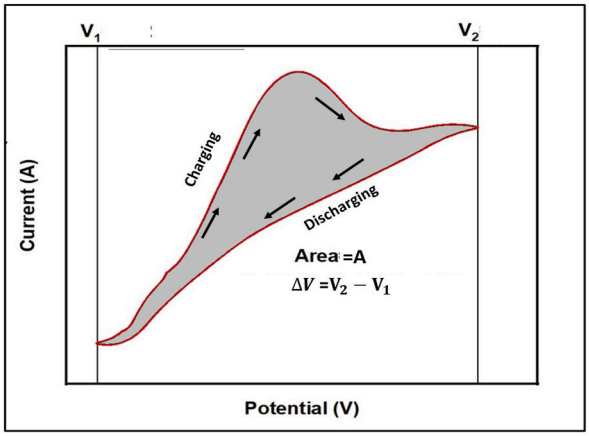

Fig. 24. Mesearment of specific capacitance (C) from CV graph.

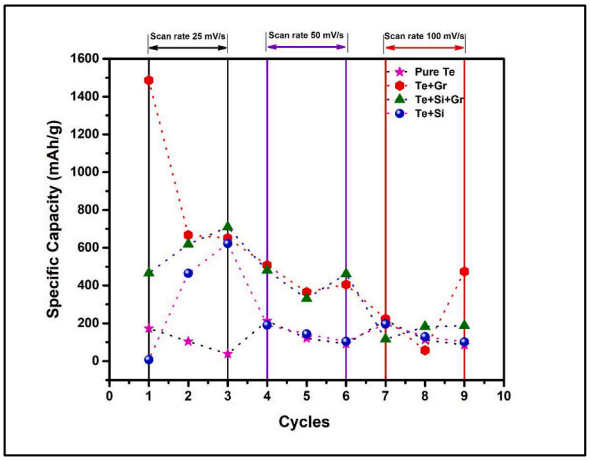

Fig. 25. Specific capacity versus cycles at different scan rate.

VI. Higher Specific capacity values in materials from CV analysis, especially when scanned at lower rates, are beneficial for battery applications. Understanding the correlation between scan rate and specific capacity values is crucial for improving electrode design and efficiency in real-world battery systems.

VII. Pure Te has a low phase angle, suitable for simpler, higher-resistance electrodes. The Te + Si sample has a harmonious resistive-capacitive combination, suitable for standard battery electrodes. Te + Gr and Te + Si + Gr exhibit higher phase angles, suggesting a greater capacitive behavior that may be well-suited for electrodes with high capacity.

VIII. Low charge transfer resistance (R_{ct}) of the Te + Gr and Te + Si + Gr samples demonstrate excellent electrode performance and high charge transfer efficiency. Furthermore, optimizing the pure Te and Te + Si samples can lead to a decrease in internal charge transfer resistance (R_{ct}) and an enhancement in charge transfer kinetics, thereby improving the battery's performance.

5. Recommendations for future research

Considering the limitations of this research work, future studies can be conducted by resolving the issues, as follows.

I. Material compositions can be improved to promote specific structural qualities. In addition, the proportions of additives can be optimized to enhance both crystallinity and grain size.

II. Surface oxidation can be reduced using an inert environment for the improvement of electrochemical stability and cycle efficiency of the tellurium-based anode.

III. Charge storage capacity, stability, and charge transfer kinetics can be altered by optimizing electrode composition and shape. Further studies can be carried out to investigate the influence of specific capacity values, including material interactions, electrolyte composition, and electrode design to enhance the battery performance.

Table 8
The Specific Capacity (Cp) and Charge (Q/m) Values When Sodium Chloride (NaCl) was used as the Electrolyte.

Sample Name	Scan rate (mV/s)	Cycle no.	Specific Capacity (Cp) (mAh/g) from CV test	Charge (Q/m) (C/g) from CV test
Pure Te	25	01	173.11	0.48
		02	104.53	0.29
		03	38.03	0.10
	50	01	212.40	0.59
		02	120.57	0.33
		03	90.97	0.25
	100	01	216.40	0.60
		02	112.51	0.31
		03	84.96	0.23
Te + Gr	25	01	1486.91	4.13
		02	667.36	1.85
		03	651.19	1.80
	50	01	507.71	1.41
		02	365.88	1.01
		03	405.08	1.12
	100	01	223.32	0.62
		02	57.57	0.15
		03	474.47	1.32
Te + Si + Gr	25	01	465.48	1.29
		02	618.82	1.71
		03	709.23	1.97
	50	01	480.10	1.33
		02	330.67	0.92
		03	460.92	1.28
	100	01	116.15	0.32
		02	182.32	0.50
		03	186.96	0.51
Te + Si	25	01	7.86	0.02
		02	464.76	1.29
		03	621.93	1.72
	50	01	190.73	0.52
		02	143.79	0.39
		03	103.71	0.28
	100	01	196.04	0.54
		02	129.57	0.35
		03	101.13	0.28

Table 9
The equivalent series resistance (R_S) and the charge transfer resistance (R_{ct}) of all tested samples.

Sample Name	The equivalent series resistance (ESR) or bulk resistance, denoted as (R_S)	The charge transfer resistance (R_{ct})
Pure Te	29.99 Ω	759.07 Ω
Te + Gr	28.13 Ω	4.21 Ω
Te + Si + Gr	30.53 Ω	36.39 Ω
Te + Si	44.05 Ω	164.905 Ω

IV. Additional research can be conducted at different aspects, including, the composition of electrodes, formulation of electrolytes, or design of electrode/electrolyte interfaces to decrease the values of R_S and R_{ct}. The correlation between phase angle, electrode structure, and electrochemical performance can be established. Apart from this, the design and composition of electrodes can be evaluated by considering impedance characteristics to boost the performance and efficiency of batteries. Moreover, the correlation between phase angle, electrode structure, and electrochemical performance can be established. In addition, the design and composition of electrodes can be changed by taking into consideration impedance characteristics to boost the performance and efficiency of batteries.

V. Only one sample (Te + Si + Gr) was contaminated by aluminum as an impurity during the preparation for TEM testing, with the aluminum mass percentage reporting below one percent (0.93 %). The small concentration of aluminum did not significantly impact the electrochemical performance of the sample. In contrast, oxygen was present as a result of surface oxidation, while sodium was included during the sample preparation for both TEM and XPS analyses. The sodium atomic percentage in the TEM study varied from 12.56 % to 18.28 %, whereas in the XPS test, it ranged from 11.36 % to 23.18 %. An increased concentration of these contaminants may affect the sample's electrochemical performance. These are the constraints of this investigation. Even so, we pursued assistance from other research organizations within the Bangladesh Council of Scientific and Industrial Research (BCSIR) as a result of the university's inability to provide the requisite testing facilities. In order to fully investigate the potential of tellurium-based samples in industrial applications, it is recommended that future researchers take more caution in the preparation and analysis of these samples during physical analysis.

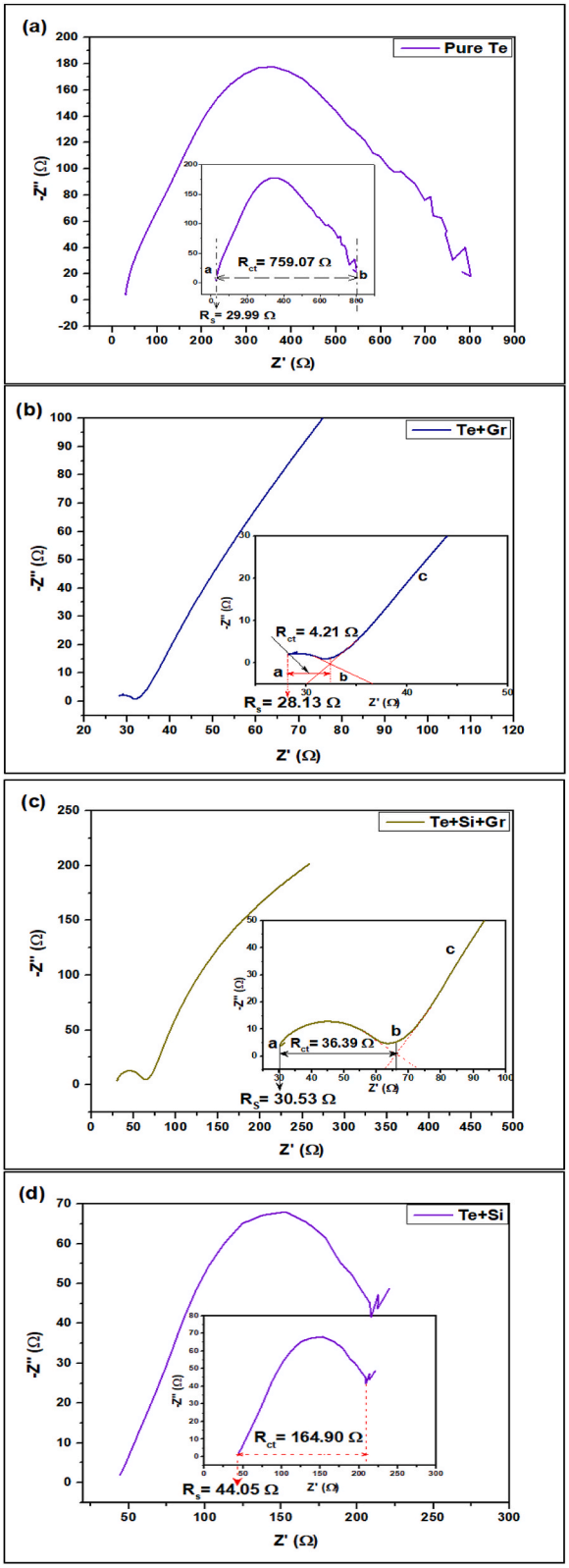

Fig. 26. Eis data of electrodes (a) pure Te (b) Te + Gr (c) Te + Si + Gr and (d) Te + Si.

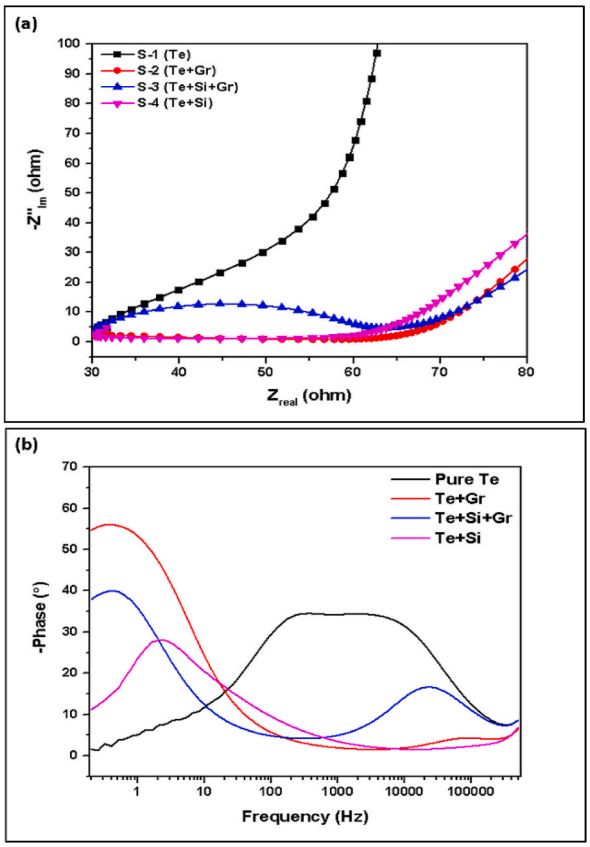

Fig. 27. Electrochemical impedance spectroscopy (EIS) curves: (a) Nyquist plot (b) phase angle.

Table 10
The table illustrates the comparison of present and previous studies of this research.

Property	Present Study				Previous Study	
TEM	Pure Te the interplanar spacing of the nanocrystal is 0.417 nm, 0.395 nm, 0.443 nm. Te + Gr the interplanar spacing of the nanocrystal is 0.307 nm, 0.308 nm, 0.335 nm. Te + Si + Gr the interplanar spacing of the nanocrystal is 0.396 nm, 0.424 nm. Te + Si the interplanar spacing of the nanocrystal is 0.224 nm, 0.229 nm.				The interplanar spacing of the Tellurium nanocrystal is 0.235 and 0.206 nm [46].	
TGA&DSC	Sample Name	Temperature (0–700 °C)			The Te content in the composite (Te@MPC) was determined to be 68.0 wt % by thermogravimetric analysis (TGA). Temperature ranges from 0 to 700 °C [47]. Note: Microporous Carbon (MPC)	
	Pure Te	61.66 wt%				
	Te + Si + Gr	49.86 wt%				
	Te + Si	50.94 wt%				
	Te + Si	44.82 wt%				
CV	Scan rate (mV/s)				Scan rate (mV/s)	
	Sample Name	25 mV/s	50 mV/s	100 mV/s	Sample Name	10–50 mV/s
	Pure Te	709.23 mAh/g	480.10 mAh/g	186.96 mAh/g	SeCoOTe/F	752.95C/g or 209.15 mAh/g [48]
	Te + Gr	621.93	190.73	196.04	SCoOTe/NF	512.40C/g or 142.33 mAh/g [48]
	Te + Si + Gr	173.11	212.40	216.40	CoOTe/NF	485.15C/g or 134.76 mAh/g [48]
	Te + Si	1486.91	507.71	474.47	Note-(1 mAh/g = 3.6C/g)	
					Ti_5Te_4/P@C	440 mAh/g [49]
					Ti_5Te_4/P(30 wt%)@C	300 mA/g [49]
EIS	Charge transfer resistance (R_{ct})				Charge transfer resistance (R_{ct})	
	Sample Name				P-CoOTe/NF 18.5 Ω [48]	
	Pure Te	759.07 Ω			CoOTe/NF 20.99 Ω [48]	
	Te + Gr	4.21 Ω				
	Te + Si + Gr	36.39 Ω				
	Te + Si	164.905 Ω				

VI. In the future, the feasibility of using this developed material as an anode for practical battery fabrication and commercial applications will be investigated, with a focus on long cycle stability and specific capacity. Additionally, its performance can be assessed for any potential issues using a commercially available battery cycler.

CRediT authorship contribution statement

Md Masud Rana: Writing – original draft, Methodology, Investigation, Formal analysis, Conceptualization. **Mohammad Asaduzzaman Chowdhury:** Writing – review & editing, Supervision, Methodology, Investigation, Formal analysis, Conceptualization. **Md. Jonaidul Alam:** Writing – review & editing, Methodology, Investigation. **Md. Rifat Khandaker:** Writing – review & editing, Methodology, Investigation. **Yusuf Ali:** Writing – review & editing, Methodology.

Data availability statement

Data will be made available on request.

Declaration of competing interest

The authors declare that they have no known competing financial interests or personal relationships that could have appeared to influence the work reported in this paper.

References

[1] A. Raihan, M. Rashid, L.C. Voumik, S. Akter, M.A. Esquivias, The dynamic impacts of economic growth, financial globalization, fossil fuel, renewable energy, and urbanization on load capacity factor in Mexico, Sustainability 15 (18) (2023) 13462.
[2] M. Farghali, et al., Social, environmental, and economic consequences of integrating renewable energies in the electricity sector: a review, Environ. Chem. Lett. 21 (3) (2023) 1381–1418.
[3] K. Raut, A. Shendge, J. Chaudhari, R. Lamba, N.F. Alshammari, Modeling and simulation of photovoltaic powered battery-supercapacitor hybrid energy storage system for electric vehicles, J. Energy Storage 82 (2024) 110324.
[4] E.E. Michaelides, V.N. Nguyen, D.N. Michaelides, The effect of electric vehicle energy storage on the transition to renewable energy, Green Energy and Intelligent Transportation 2 (1) (2023) 100042.
[5] J. Xu, et al., High-energy lithium-ion batteries: recent progress and a promising future in applications, Energy & Environmental Materials 6 (5) (2023) e12450.
[6] J. Liu, et al., Advances and prospects in improving the utilization efficiency of lithium for high energy density lithium batteries, Adv. Funct. Mater. 33 (34) (2023) 2302055.
[7] G. Zhu, D. Luo, X. Chen, J. Yang, H. Zhang, Emerging multiscale porous anodes toward fast charging lithium-ion batteries, ACS Nano 17 (21) (2023) 20850–20874.
[8] B.M. Khan, W.C. Oh, P. Nuengmatch, K. Ullah, Role of graphene-based nanocomposites as anode material for Lithium-ion batteries, Mater. Sci. Eng., B 287 (2023) 116141.
[9] H. Ahmed, Synthesis and Characterization of Silicon-Carbon Composites as Anode Materials for Li-Ion Batteries, 2023.
[10] H.G. Ali, et al., Advancements in two-dimensional materials as anodes for lithium-ion batteries: exploring composition-structure-property relationships emerging trends, and future perspective, J. Energy Storage 73 (2023) 108980.
[11] M. Kim, J. Park, J. Baek, H. Son, G. Lee, Optimizing the performance of a graphite anode for innovative metal-ion batteries and hybrid capacitors, J. Power Sources 603 (2024) 234396.
[12] Y. Xiao, Y. Mao, T. Li, X. Hao, W. Wang, Facile synthesis of a SiO x-graphite composite toward practically accessible high-energy-density lithium-ion battery anodes, ACS Appl. Mater. Interfaces 15 (39) (2023) 45938–45948.
[13] C. Lamiel, I. Hussain, H. Rabiee, O.R. Ogunsakin, K. Zhang, Metal-organic framework-derived transition metal chalcogenides (S, Se, and Te): challenges, recent progress, and future directions in electrochemical energy storage and conversion systems, Coord. Chem. Rev. 480 (2023) 215030.
[14] X. Wang, L. Liu, Z. Hu, C. Peng, C. Han, W. Li, High energy density aqueous zinc–chalcogen (S, Se, Te) batteries: recent progress, challenges, and perspective, Adv. Energy Mater. 13 (44) (2023) 2302927.
[15] H.W. Yang, J.H. Yoo, J. Hur, Y.N. Ahn, I.T. Kim, Mechanically robust and conductive Ti5Te4/P@ C composite materials as promising lithium-ion battery anodes, J. Energy Storage 86 (2024) 111218.
[16] W.S. Choi, M. Kim, I.T. Kim, Te-rP-C anodes prepared using a scalable milling process for high-performance lithium-ion batteries, Micromachines 14 (12) (2023) 2156.
[17] Wenmiao Zhao, Xiaoyuan Shi, Bo Liu, Hiroshi Ueno, Ting Deng, Weitao Zheng, The design and engineering strategies of metal tellurides for advanced metal-ion batteries, J. Energy Chem. 89 (2024) 579–598.
[18] M. Ahmad, et al., Evolution of metal tellurides for energy storage/conversion: from synthesis to applications, Small (2024) 2310099.
[19] Jing-Kai Qin, Chao Sui, Zhao Qin, Jianyang Wu, Hua Guo, Zhen Liang, Cheng-Yan Xu, et al., Mechanical anisotropy in two-dimensional selenium atomic layers, Nano Lett. 21 (19) (2021) 8043–8050.
[20] Shuai Dong, Dandan Yu, Jie Yang, Li Jiang, Jiawei Wang, Liwei Cheng, Yan Zhou, Honglei Yue, Hua Wang, Lin Guo, Tellurium: a high-volumetric-capacity potassium-ion battery electrode material, Adv. Mater. 32 (23) (2020) 1908027.
[21] H. Su, X. Li, C. Liu, Y. Shang, H. Liu, Scalable synthesis of micrometer-sized porous silicon/carbon composites for high-stability lithium-ion battery anodes, Chem. Eng. J. 451 (2023) 138394.
[22] Z. Yan, S. Yi, X. Li, J. Jiang, D. Yang, N. Du, A scalable silicon/graphite anode with high silicon content for high-energy lithium-ion batteries, Mater. Today Energy 31 (2023) 101225.
[23] H. Liu, et al., The application road of silicon-based anode in lithium-ion batteries: from liquid electrolyte to solid-state electrolyte, Energy Storage Mater. 55 (2023) 244–263.
[24] Q. Zhang, et al., A silicon/carbon/reduced-graphene composite of honeycomb structure for high-performance lithium-ion batteries, J. Alloys Compd. 944 (2023) 169185.
[25] G. Liu, et al., High-performance dual-ion battery based on silicon–graphene composite anode and expanded graphite cathode, Molecules 28 (11) (2023) 4280.
[26] N. Kim, Y. Kim, J. Sung, J. Cho, Issues impeding the commercialization of laboratory innovations for energy-dense Si-containing lithium-ion batteries, Nat. Energy 8 (9) (2023) 921–933.
[27] M. Je, D.-Y. Han, J. Ryu, S. Park, Constructing pure Si anodes for advanced lithium batteries, Accounts of Chemical Research 56 (16) (2023) 2213–2224.
[28] Y. Zhang, D. Manaig, D.J. Freschi, J. Liu, Materials design and fundamental understanding of tellurium-based electrochemistry for rechargeable batteries, Energy Storage Mater. 40 (2021) 166–188.

[29] D. Petrushenko, et al., Dip-coating of carbon fibers for the development of lithium iron phosphate electrodes for structural lithium-ion batteries, Energy & Fuels 37 (1) (2022) 711–723.
[30] D. Yu, et al., Subnano-sized tellurium@ nitrogen/phosphorus co-doped carbon nanofibers as anode for potassium-based dual-ion batteries, Chem. Eng. J. 454 (2023) 139908.
[31] Hafiza Sana Rafiq, Batool Fatima, Dilshad Hussain, Abrar Mohyuddin, Saadat Majeed, Sumaira Manzoor, Muhammad Imran, et al., Selective electrochemical sensing of hemoglobin from blood of β-thalassemia major patients by tellurium nanowires-graphene oxide modified electrode, Chem. Eng. J. 419 (2021) 129706.
[32] B. Gonçalves, C. Exposito, T.T. Ishikawa, G.Y. Koga, X-ray diffraction study of the early hydration of Portland cements containing calcium carbonate by in-situ and ex-situ approaches, Construct. Build. Mater. 365 (2023) 129947.
[33] R. Moreira, L.P. dos Santos, C. Salomão, E.B. Barros, I.F. Vasconcelos, Influence of grain boundaries on nanoscale charge transport properties of transparent conductive ZnO-based electrodes, ACS Appl. Electron. Mater. 6 (1) (2023) 415–425.
[34] M. Shreevalli, et al., X-Ray Diffraction line profile analysis of defects and precipitates in high displacement damage neutron-irradiated austenitic stainless steels, Nucl. Eng. Technol. 56 (1) (2024) 114–122.
[35] K. Patel, A. Patel, V.P. Jethwa, H. Patel, G. Solanki, X-ray diffraction analysis of Orthorhombic SnSe nanoparticles by Williamson-Hall, Halder-Wagner and Size-Strain plot methods, Chemical Physics Impact (2024) 100547.
[36] S.-W. Chen, Y. Chen, J.R. Chang, H.-j. Wu, Co/GeTe interfacial reactions and Co-Ge-Te phase equilibria, J. Taiwan Inst. Chem. Eng. 146 (2023) 104890.
[37] M. Sudheer, P. Rani, S.P. Patole, P.S. Alegaonkar, Thermophysical assessments on self-assembled tellurium nanostructures, J. Phys. Chem. C 127 (36) (2023) 18076–18088.
[38] Yujie Xia, Lei Peng, Le Shu, Ao Wu, Hezhu Shao, Ben Li, Juan Zhang, Zhan Sui, Heyuan Zhu, Strong Intervalley Scattering-Induced Renormalization of Electronic and Thermal Transport Properties and Selection Rule Analysis in 2D Tellurium, ACS nano 18 (7) (2024) 5814–5827.
[39] A. Sinhamahapatra, J.-P. Jeon, J.-S. Yu, A new approach to prepare highly active and stable black titania for visible light-assisted hydrogen production, Energy Environ. Sci. 8 (12) (2015) 3539–3544.
[40] S. Zhang, J. Zhang, S. Xu, X. Yuan, B. He, Li ion diffusivity and electrochemical properties of FePO4 nanoparticles acted directly as cathode materials in lithium ion rechargeable batteries, Electrochim. Acta 88 (2013) 287–293.
[41] C. Yin, H. Zhou, Z. Yang, J. Li, Synthesis and electrochemical properties of LiNi0. 5Mn1. 5O4 for Li-ion batteries by the metal–organic framework method, ACS applied materials & interfaces 10 (16) (2018) 13625–13634.
[42] C. Zhao, H. Yin, Z. Yang, C. Ma, Equivalent series resistance-based energy loss analysis of a battery semiactive hybrid energy storage system, IEEE Trans. Energy Convers. 30 (3) (2015) 1081–1091.
[43] A. Lievre, A. Sari, P. Venet, A. Hijazi, M. Ouattara-Brigaudet, S. Pelissier, Practical online estimation of lithium-ion battery apparent series resistance for mild hybrid vehicles, IEEE Trans. Veh. Technol. 65 (6) (2015) 4505–4511.
[44] Z. Zhang, et al., Exploration of fast ion diffusion kinetics in graphene nanoscrolls encapsulated CoSe2 as advanced anode for high-rate sodium-ion batteries, Carbon 181 (2021) 69–78.
[45] K. Li, et al., Phosphorus vacancy regulation and interfacial coupling of biotemplate derived CoP@ FeP2 heterostructure to boost pseudocapacitive reaction kinetics, Chem. Eng. J. 454 (2023) 140223.
[46] Hongliang Zhu, Li Fan, Kaili Wang, Hao Liu, Jiawei Zhang, Shancheng Yan, Progress in the synthesis and application of tellurium nanomaterials, Nanomaterials 13 (14) (2023) 2057.
[47] Juan Zhang, Ya-Xia Yin, Ya You, Yang Yan, Yu-Guo Guo, A high-capacity tellurium@ carbon anode material for lithium-ion batteries, Energy Technol. 2 (9–10) (2014) 757–762.
[48] Mani Sakthivel, Kuo-Chuan Ho, X-CoOTe (X= S, Se, and P) with oxygen/tellurium dual vacancies and banana stem fiber-derived carbon fiber as battery-type cathode and anode materials for asymmetric supercapacitor, ACS Appl. Mater. Interfaces 16 (15) (2024) 18754–18767.
[49] Hye Won Yang, Ji Hyeon Yoo, Jaehyun Hur, Yong Nam Ahn, Il Tae Kim, Mechanically robust and conductive Ti5Te4/P@ C composite materials as promising lithium-ion battery anodes, J. Energy Storage 86 (2024) 111218.